POLITECNICO DI TORINO

Master's Degree in Mechanical Engineering

Master's Degree Thesis

Test Bench Design and Contact Model Analysis for Pyroshock Testing

Supervisors	Candidate
Prof. Alessandro Fasana	Federico Pavone
Dr. Luca Viale	

July 2024

Summary

Recent advancements in the space sector, such as the active involvement of private investors and the integration of reusable launchers, have driven down the costs associated with space missions, leading to a surge in spacecraft launches.

Spacecraft testing plays an essential role in the pre-deployment phase, particularly in mitigating the risks of failure of critical components associated with violent events such as shocks experienced during launch and deployment; those shocks come mainly from devices that are used extensively in space, namely pyrotechnic devices.

Physical tests to simulate pyrotechnic shocks are common and well documented by different standards, but often require iterative and time-consuming setup and calibration processes. Addressing these challenges, research initiatives by members of the Dynamics of Mechanical Systems and Identification Laboratory of Politecnico di Torino have focused on developing parametric models capable of overcoming such limitations.

This thesis aims to explain the author's contribution to the development of a test platform designed to gather extensive data, essential for refining and validating such models. In particular, this activity focused on the structural verification of the frame supporting the resonant plate according to European standards and the design of a safety device for the test bench.

Additionally, analyzing a pre-existing dataset, it is proposed an approach for extracting pertinent features from the data obtainable from the test bench and correlate them with testing characteristics, and compare different contact models to assess their reliability in modelling a particular set of impacts.

Table of Contents

List of Tables

List of Figures

Nomenclature

Acronyms:

ECSS European Cooperation for Space Standardization

ESA European Space Agency

SRS Shock Response Spectrum

SDOF Single Degree of Freedom

DOE Design of Experiment

List of Symbols:

W Work

m Mass

$\mathbf{a}$ Acceleration

$\mathbf{d}$ Displacement

Q Quality factor

ζ Damping

f Frequency

F_{max} Maximum force

t_c Time of contact

ρ Density

ν Poisson's ratio

E Young's modulus

R Object radius

e Coefficient of restitution

E_k Kinetic energy

p Momentum

τ Period

$F_{p,Cd}$ Force preload

f_{ub} Ultimate tensile strength

A_s Section area

γ_M Safety factor

$\sigma^g{}_\perp$ Normal stress perpendicular to the weld throat

$\tau^g{}_\perp$ Shear stress perpendicular to the axis of the weld

$\tau_\parallel^g$ Shear stress parallel to the axis of the weld

β_w Correlation factor

r Distance with neutral axis

I Moment of area

σ_t Tension stress

$F_{t,Ed}$ Tension force

$F_{t,Rd}$ Tension resistance

$F_{v,Ed}$ Shear force

$F_{s,Rd}$ Shear resistance

$F_{b,Rd}$ Bearing resistance

t_{max} Time of force peak

t_l Instant of time in which the contact starts

t_r Instant of time in which the contact ends

Chapter 1

Introduction

The purpose of this introduction is to provide the reader with a general understanding of the space sector nowadays and the possible benefits that can be gained from the testing method that will be illustrated later.

The state of the art of a specific testing technique is given, accompanied by the description of a novel method to simulate such tests and a review of contact models, useful to understand the current limitations.

1.1 Space Economy

In recent years, a series of revolutions in the space sector, such as the opening of the field to private investors and the use of reusable launchers, has significantly decreased the costs of space missions, making the low Earth orbit accessible not only for defence and government purposes, but also for more general applications possible thanks to satellites, that range from Earth observation studies, to telecommunication and internet providers.

As a result, the number of spacecrafts sent from Earth has literally skyrocketed.

Even if the United States is by far the largest player with a number of spacecrafts almost ten times higher than any other nation, in the European Union there is a vibrant colony of start-ups and some large state-owned enterprises, whose field of expertise range from building launchers to providing software services for satellites.

In order to facilitate the collaboration, ensure reliability, safety and interoperability of space systems and components, the European Space Agency (ESA) has redacted a series of standards over the years known as “European Cooperation for Space Standardization” (ECSS). These standards, that regulate every step of the lifecycle of a spacecraft, will be referred to in this paper to describe technical aspects.

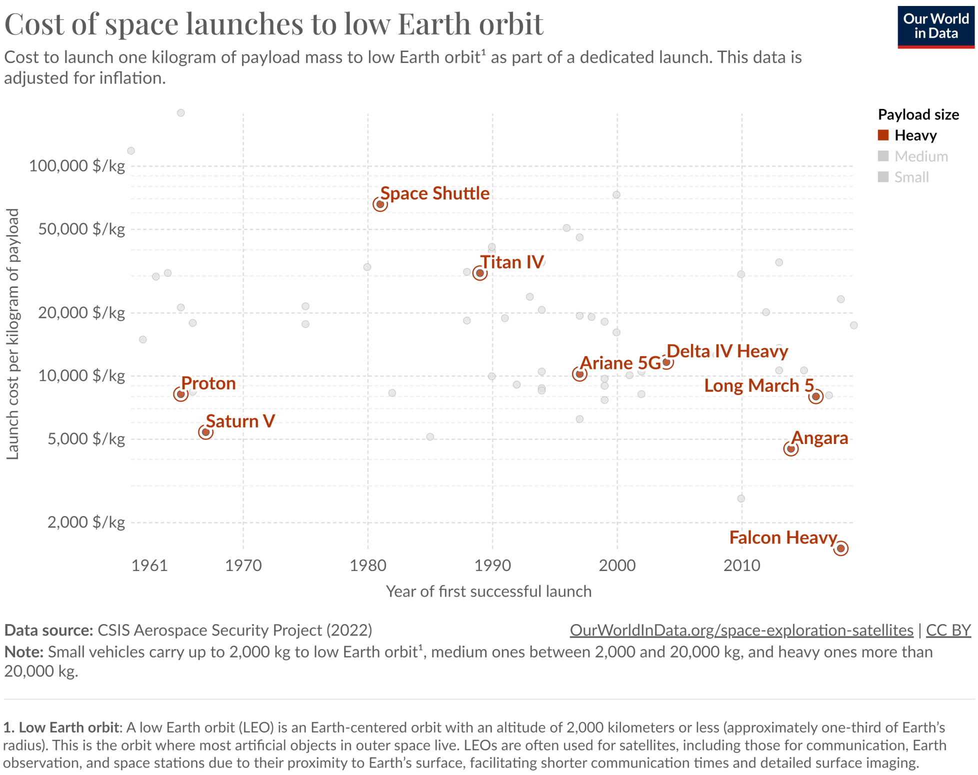

Cost of space launches to low Earth orbit

Cost to launch one kilogram of payload mass to low Earth orbit[1] as part of a dedicated launch. This data is adjusted for inflation.

Data source: CSIS Aerospace Security Project (2022) OurWorldInData.org/space-exploration-satellites | CC BY

Note: Small vehicles carry up to 2,000 kg to low Earth orbit[1], medium ones between 2,000 and 20,000 kg, and heavy ones more than 20,000 kg.

[1] **Low Earth orbit**: A low Earth orbit (LEO) is an Earth-centered orbit with an altitude of 2,000 kilometers or less (approximately one-third of Earth's radius). This is the orbit where most artificial objects in outer space live. LEOs are often used for satellites, including those for communication, Earth observation, and space stations due to their proximity to Earth's surface, facilitating shorter communication times and detailed surface imaging.

Figure 1.1: Cost per kilogram of space launches to LEO [1]

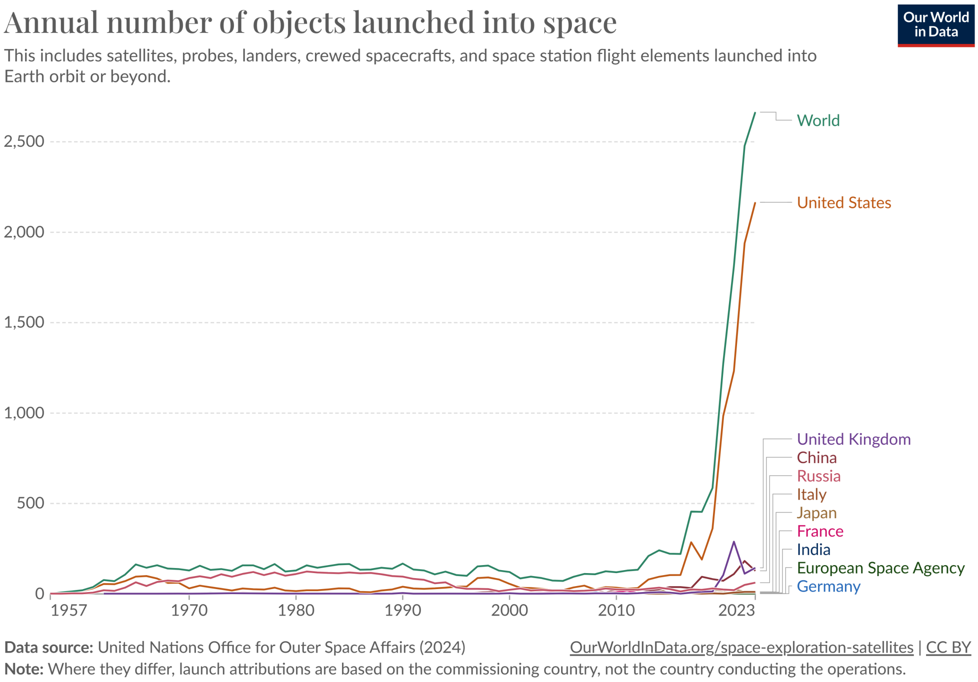

Annual number of objects launched into space

This includes satellites, probes, landers, crewed spacecrafts, and space station flight elements launched into Earth orbit or beyond.

Data source: United Nations Office for Outer Space Affairs (2024) OurWorldInData.org/space-exploration-satellites | CC BY

Note: Where they differ, launch attributions are based on the commissioning country, not the country conducting the operations.

Figure 1.2: Annual number of objects launched into space [1]

1.2 Spacecraft testing

Before reaching their final destination, be it the Low Earth Orbit (LEO), at approximately 2000 kilometres from earth, or the depth of space of the probe Voyager 1, at about 24 billion kilometres from Earth, every spacecraft must endure a series of violent events that can irremediably damage vital components. The most dangerous of these events happen during the first phase of the mission, from launch to the various separation stages.

In this work, attention will be focused on a particular set of events called shocks, characterised by short duration and high force peaks, as will be illustrated later.

According to the Ariane 5 user manual [2], the main sources of shocks are represented by the following events:

- the launch vehicle upper stage separation from the main cryogenic stage
- the fairing jettisoning
- the spacecraft separation

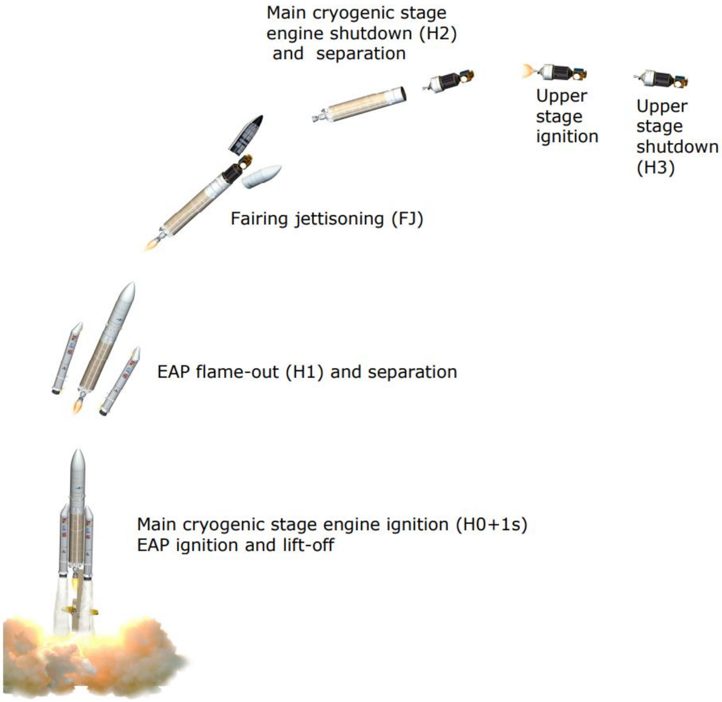

Figure 1.3: Ariane 5 typical sequence of events [2]

Depending on the specific mission and payload, a series of additional pyrotechnic devices can be used to release different instruments.

The physics behind the different devices is in most cases the same: an electrical input generates a chemical reaction that releases energy in the form of pyrotechnic output. Depending on the configuration, additional energy, usually stored in mechanical components such as compressed springs, is simultaneously released to perform the required task.

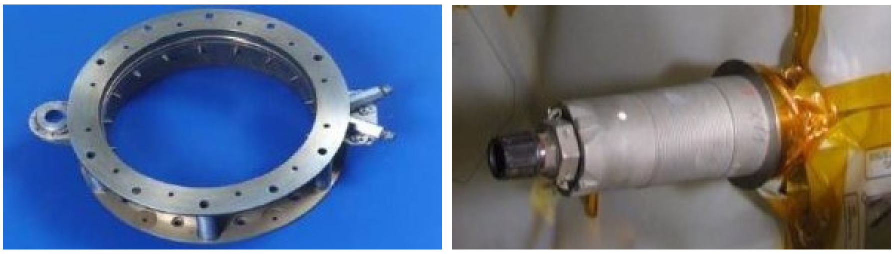

(a) Ariane 5 micro satellite separation system

(b) Dnepr explosive bolts

(c) PSLV separation system

(d) NASA Standard Initiator

Figure 1.4: Pyrotechnic separation systems [3]

The ECSS-E-HB-32-25A standard [3] defines a flowchart to determine if, and what type of test has to be performed in order to evaluate the fitness for space regarding shock (fig. 1.5).

Due to the difficulties in simulating high frequency shocks, physical tests are usually adopted as a qualification method, but the set up and calibration is frequently an iterative and rather time-consuming activity.

The development of a parametric model capable of overcoming such limitations has been the focus of different articles published by the members of the Dynamics of Mechanical Systems and Identification Laboratory of Politecnico di Torino [4] [5] [6].

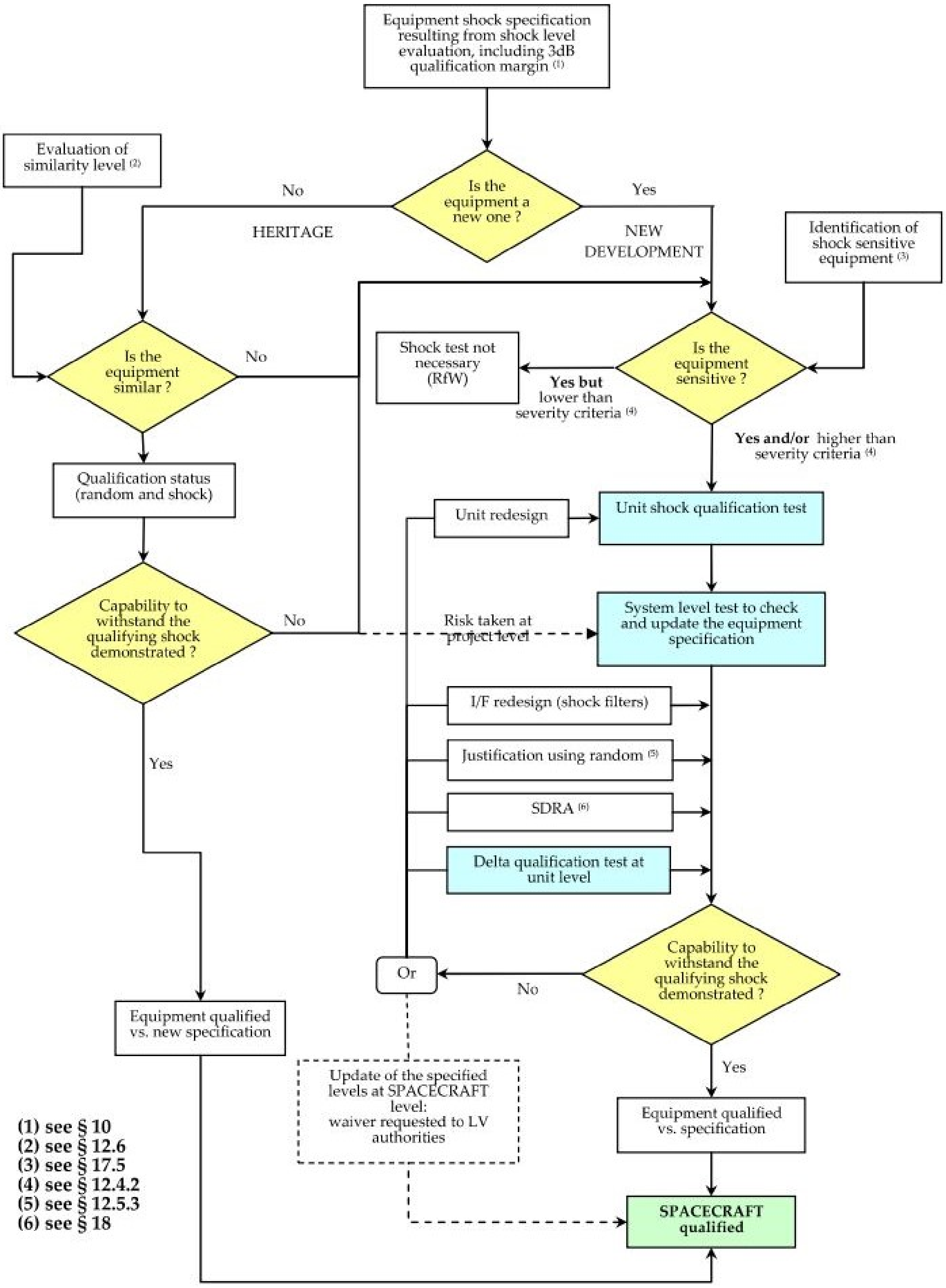

Figure 1.5: Flowchart for shock verification qualification [3]

1.3 Pyroshock tests

1.3.1 Shock

In the field of dynamics, according to *The Science and Engineering of Mechanical Shock* [7], a shock event can be described as a dynamic loading whose duration is short relative to the natural frequency of the excited system.

To provide context, an automobile crash can generate an acceleration of 20-100 g and has a duration of 0.1 s, while a pyrotechnic shock produces 1000-100,000 g and has a duration in the order of 0.001 s [7].

The work W provided during the shock events can be defined, according to Newton's laws, as:

$$W = m\,\mathbf{a} \cdot \mathbf{d} \tag{1.1}$$

Where m is the mass of the system, $\mathbf{a}$ the acceleration and $\mathbf{d}$ the displacement.

It is clear that, for a given amount of input energy, acceleration and displacement are inversely proportional. Therefore, low acceleration shocks tend to cause high displacements, while high acceleration shocks result in reduced displacements [7].

These solicitations, although not among the most dangerous for structural parts, are critical for electronic components, functional mechanical assemblies and mechanisms [3].

Standards such as ECSS-E-HB-32-25A [3] provide frameworks for understanding shock environments for space components dimensioning. This standard highlights the key distinction between shock and standard vibration: a shock has an excitation duration which is significantly shorter than the response time of the equipment, and then the system responds freely. On the other side a vibration environment has an excitation duration which is long compared to the response time of the equipment. For that reason, the system response to a shock is better described by the propagation of elastic waves that interact with boundary conditions and geometry of the system in a complex way.

Depending on the relative position of the source and the system, the shock environment can be classified in three main types:

- Near field environment: direct wave propagation, high accelerations and frequency; the system is located around a dozen of centimetres from the source.

- Mid field environment: combination of the propagating waves and the structural resonances due to reflecting waves in the structure; lower acceleration than near field environment but still high frequency content. The source is located from dozen to several dozens of centimetres from the system.

- Far field environment: the excitation comes from structural resonance due to reflecting waves; characterised by reduced accelerations (up to a fifth of the values in the near-field) and low frequency content. Located outside the mid-field area.

To analyse shock events in more detail, the standard instrument adopted in pyroshock testing is the Shock Response Spectrum (SRS).

1.3.2 Shock Response Spectrum

The Shock Response Spectrum (SRS) is calculated starting from an input transient in time domain and is a function that allows characterizing the effect that a shock induces on a standardized dynamical system in order to estimate the severity and damaging potential. The SRS can be used to compare shocks and establish equivalence criterion between a measured transient in the application domain and a laboratory simulation of that environment [3].

The method to calculate the SRS is well documented in various technical standards; as an example, the European standard ECSS defines the following procedure:

- Defining an array of single degree of freedom systems (SDOF), characterised by their natural frequencies f_n, with a quality factor $Q = 10$, assuming a conventional damping $\zeta = 5\%$ ($Q = \frac{1}{2\zeta}$). The set of SDOF systems is arbitrary, however a common scheme is to choose a proportional bandwidth of separation of 1/24 octave ($f_n = f_{n-1}2^{\frac{1}{24}}$) and a range of 100 Hz - 100 kHz for near field time sources and 100 Hz - 10 kHz for medium or far-field time sources.

- Applying to the set of SDOF systems a time history input as a base excitation;

- Calculating for each SDOF systems the temporal maximum of the response; the response can be in terms of displacement, velocity or acceleration, depending on the input, with the last one widely used in the aerospace sector.

- Draw a graph of the maximum response amplitude (at any time and any directions) as a function of the frequencies of the SDOF systems.

The result is the so-called maximax SRS, which is one of the most usually adopted in space qualification processes.

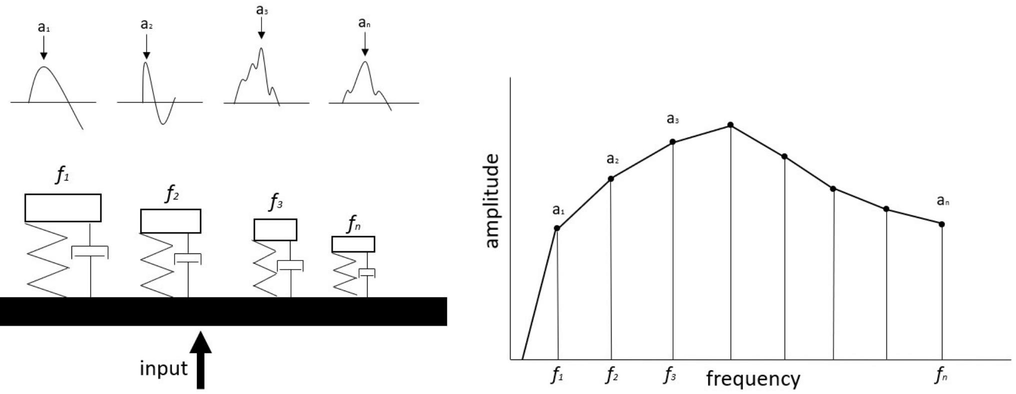

(a) SDOF systems and response **(b)** maximax SRS

Figure 1.6: SRS calculation procedure

It is a responsibility of the launcher manufacturer or the specific mission management to define a requirement in terms of shock environment produced, while the test tolerance is defined by technical standards as the ECSS-E-ST-10-03C, that indicates an amplitude tolerance of $-3dB/+6dB$ across the full spectrum.

As an example, the Ariane 5 user manual provides the following SRS for the upper stage separation and faring jettisoning at the clampband release at spacecraft interface.

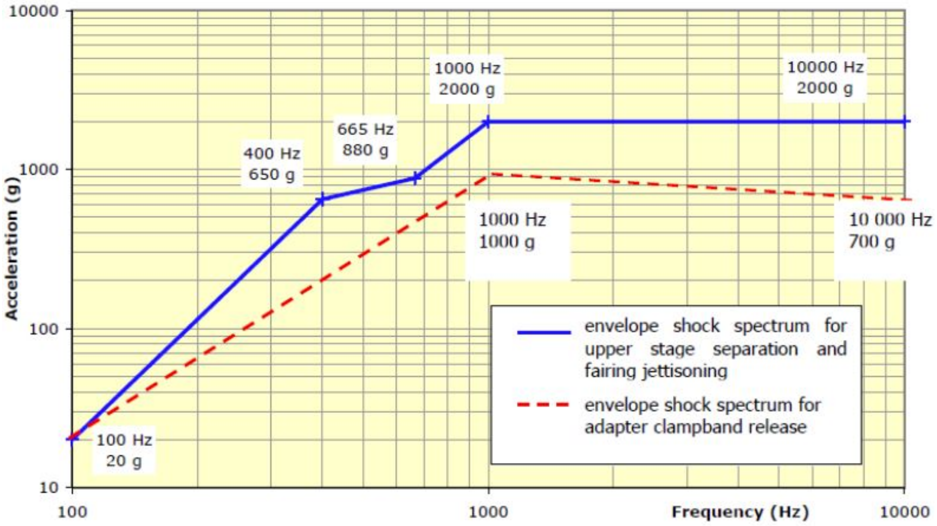

Figure 1.7: SRS for the upper stage separation, fairing jettisoning and envelope shock spectrum for clampband release at spacecraft interface, Ariane 5 [2]

1.3.3 Pyroshock test benches

The verification process aims to prove that the component can withstand the shock environment in which it will be placed. To reproduce the shock environment required by the technical standards, many configurations and test benches can be adopted.

The level at which the test is carried out is relevant: a system level test is adopted to analyse the behaviour of the entire payload, requiring large-size test benches.

An equipment level test is instead performed on single components or relatively small subsystems, making it possible to use smaller test benches.

One of the system level tests usually adopted to analyse shocks induced on the flight hardware during stage separation is the clampband release test; the actual payload is suspended on a crane and the stage separation event is simulated actuating the clampband mechanism, that can be either activated by a pyrotechnic nut or a mechanical drive. The inferior structure, which is a mock-up of the inferior stage or the rocket vector, falls down, while the payload remains suspended; sensors placed on the system register the information about the shock environment produced.

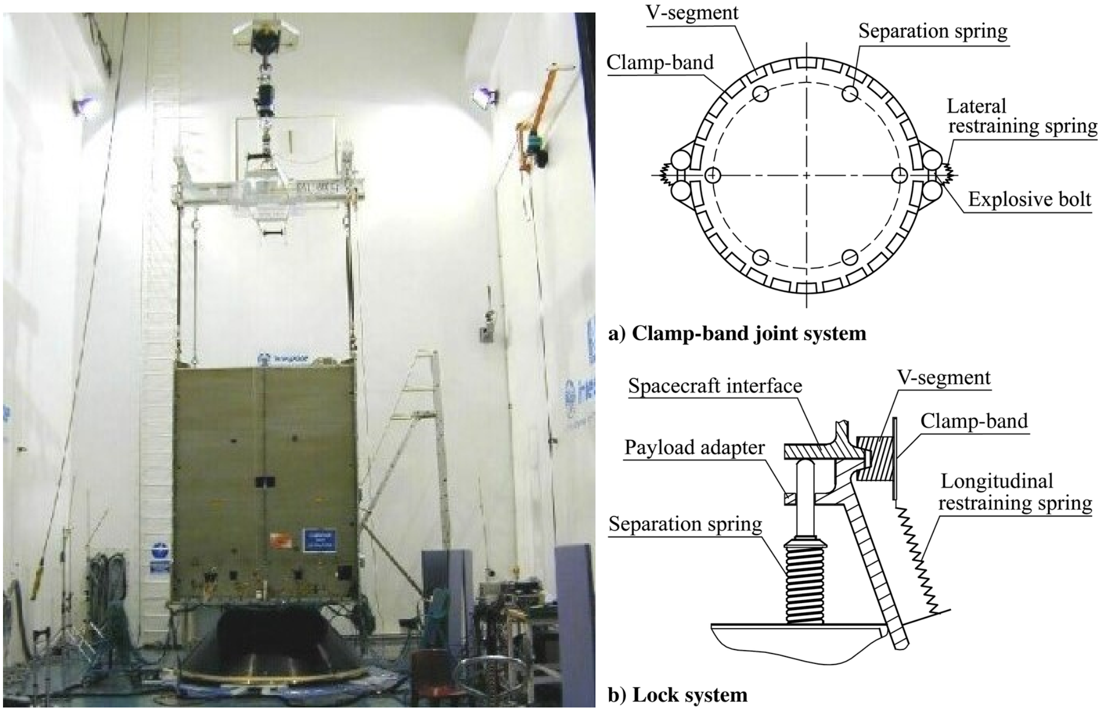

(a) (b)

Figure 1.8: Calmpband release test [3] and clampband design [8]

It is possible to categorise equipment test benches on the basis of the means of excitation [3] :

- Explosive excitation: use of an actual explosive on a controlled environment to simulate near-field shock environment;
- Mechanical excitation (metal-to-metal impact): the mid and far-field shock environment is simulated using an object impacting a resonant structure, usually a plate or a bar;
- Electrodynamic shaker: convenient because of their versatility (shock tests and random vibration tests can be conducted on the same machine) but limited in the high frequencies that can be reached.

Further insights can be given on mechanical excitation tests depending on the system configuration. One of the most common configurations involves a plate, an impacting mass and possibly an anvil component between the two. The geometry of the resonant plate influences the response to the input, as well as the constraints: the plate can be either fixed or hung to simulate different boundary conditions and generate different responses. In a typical configuration, the impacting mass can be dropped from a defined height in a pendulum-like configuration, that assures low operational cost, repeatable behaviour and easy operation. The direction of the impact (in plane or out of plane), the geometry of the plate and its constraints, the height of the mass, the position of the impact and the presence of the anvil are all variables that affects the response of the system and are thus used to calibrate the machine.

One of the properties that can be tuned by changing the geometry of the plate and its boundary conditions is the so-called “knee” of the SRS; this point is where the value of interest (acceleration in most cases) reaches a plateau and remains approximately constant at higher frequencies, as it can be seen in figure 1.7 at 1000 Hz.

For example, experimental results show that thicker and smaller (in terms of area) plates show a knee at higher frequencies [9].

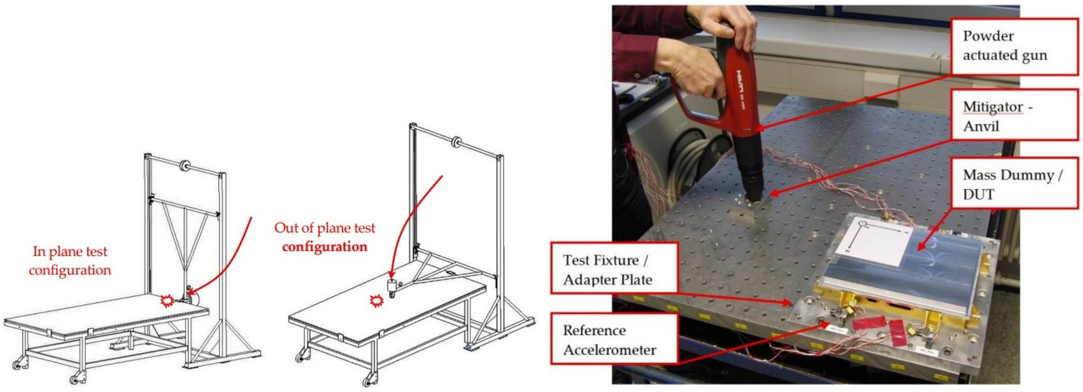

(a) Pendulum impact **(b)** Powder gun

Figure 1.9: Example of different mechanical excitation test benches [3]

While maintaining the plate as a resonant structure, shock excitation can be achieved using other means. For example, a powder-actuated gun can deliver an impulse to the plate, or a projectile can be launched using compressed air or a spring mechanism. These methods provide alternative ways to excite the plate, each with its own set of advantages and suitable applications.

Another configuration involving a resonant plate is the bi-plate technology, in which the baseplate, which remains the resonant structure that is excited, is separated from the specimen by a supporting plate, connected to the baseplate with mechanical connections (spacers, bolts). The main advantages of this configuration are the filter applied to higher frequencies by the coupling and the possibility to test heavier components [3].

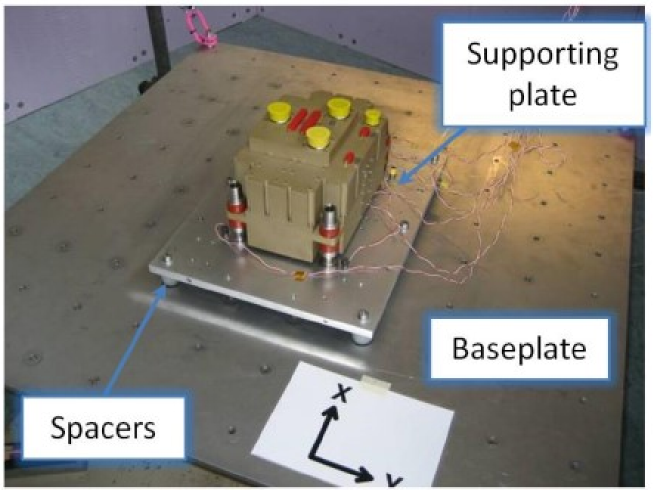

Figure 1.10: Bi-plate test bench [3]

An example of a mechanical excitation test bench that does not use a resonant plate but rather a beam is the Hopkinson beam technology. It consists of a metallic beam that is interposed between the specimen and the source of excitation; when hit, the beam's response is a damped sinus, quasi mono-frequency shock, that excites the test specimen. An interesting feature of this configuration is the possibility to tune the knee of the SRS by adjusting the position of the clamping fixtures, thus modifying the length of the free beam [10].

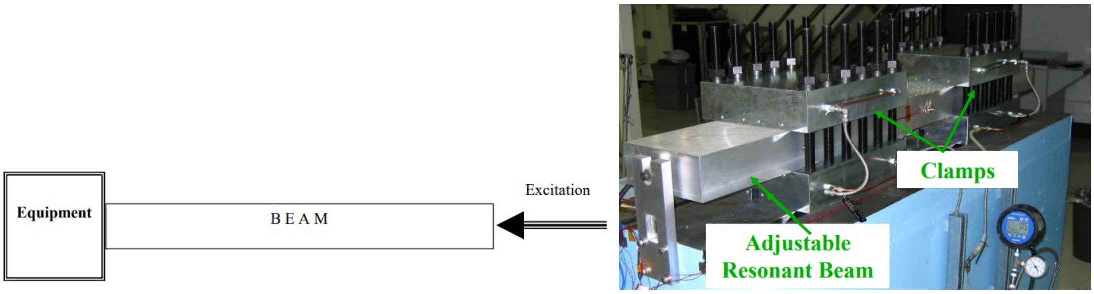

(a) (b)

Figure 1.11: Hopkinson beam and tunable test bench

1.4 Impact analysis

A parametric model capable of simulating pyroshock tests on resonant plates is currently under development in the Dynamics of Mechanical Systems and Identification Laboratory of Politecnico di Torino [6].

The proposed method integrates three consecutive phases:

- An analysis using CAD and FEM software to obtain the receptance of the plate
- The definition of the impulse
- The computation of the SRS

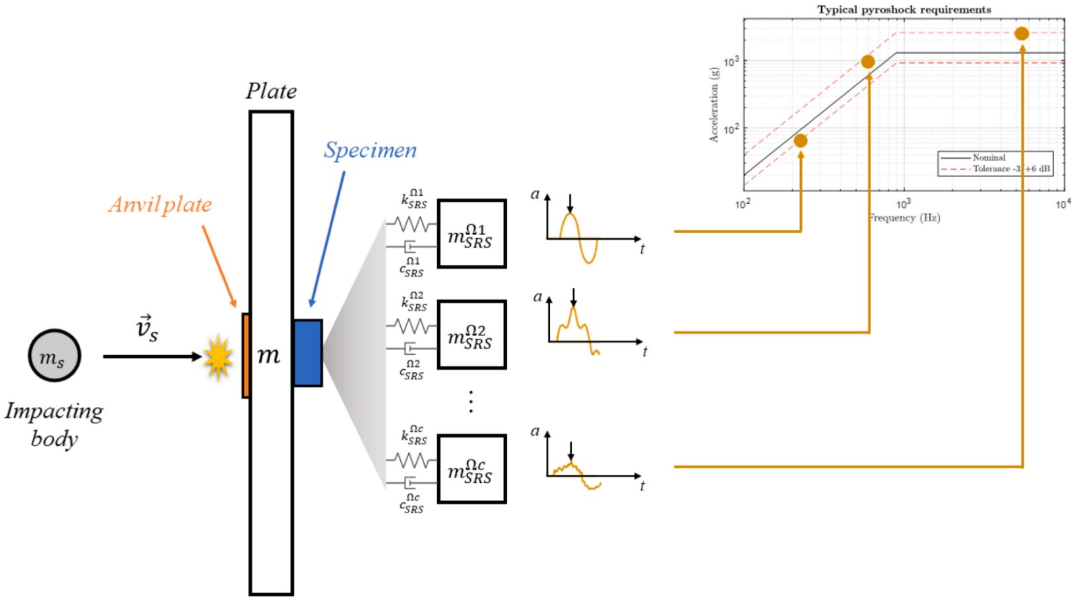

Figure 1.12: simplified model of the method proposed in [6]

Those steps, all integrated in the MATLAB environment, require as input many parameters that can be grouped into characteristics of the plate (geometry, material, boundary conditions) and impact pulse characteristics (time duration, profile shape, properties of the impacting objects) [6].

The model can be either used to solve the direct problem, namely simulating the resulting SRS given as input the testing characteristics, or solving the inverse problem obtaining as a result the testing characteristics (plate geometry, speed of impacts, etc.) given as input the required SRS.

In the predictive model, the force impulse transmitted by the impacting object on the resonant plate is a key aspect that affects the SRS characteristics; its shape, duration and other relevant properties influence largely the accuracy of the output predictions, making it necessary to investigate the physics behind the phenomenon to select an appropriate contact model.

One of the first and still one of the most used theoretical models was developed by Hertz in 1882 to study the impact between elastic bodies, in absence of friction, that collide in a quasi-static manner [11], meaning that the approaching velocity is much lower than the propagation speed of elastic waves in the bodies.

The application of this theory has gone beyond the limitations imposed by the simplifying assumptions since in many scenarios some parameters calculated show notable accordance with experimental evidences [12].

Focusing on the particular case related to the pyroshock testing techniques, it is possible to derive from Hertz's theory the impulsive force generated by an impacting sphere on a massive flat body as, according to Hunter [12]:

$$\begin{cases} F(t) = F_{max} sin(\frac{\pi t}{t_c}) & 0 \leq t \leq t_c \\ F(t) = 0 & otherwise \end{cases} \tag{1.2}$$

And the contact time is:

$$t_c = 4.53 \left[\frac{4\rho_1}{3} \left(\frac{(1-\nu_1^2)}{E_1} + \frac{(1-\nu_2^2)}{E_2} \right) \right]^{\frac{2}{5}} R_1 v_0^{-\frac{1}{5}} \tag{1.3}$$

A modified model proposed by Reed [12] raise the sine function to a power of $\frac{3}{2}$, yielding the result:

$$\begin{cases} F(t) = F_{max} sin^{\frac{3}{2}}(\frac{\pi t}{t_c}) & 0 \leq t \leq t_c \\ F(t) = 0 & otherwise \end{cases} \tag{1.4}$$

In the Reed model, in addition to the contact time calculated as in eq 1.3, the maximum force is given as:

$$F_{max} = 1.917 \rho_1^{\frac{3}{5}} \left(\frac{(1-\nu_1^2)}{\pi E_1} + \frac{(1-\nu_2^2)}{\pi E_2} \right)^{-\frac{2}{5}} R_1^2 v_0^{\frac{6}{5}} \tag{1.5}$$

Where, in both models, ρ_1 is the density of the impacting object, R_1 is radius, and v_0 the approach velocity; ν_i and E_i are the Poisson's ratio and the Young's modulus.

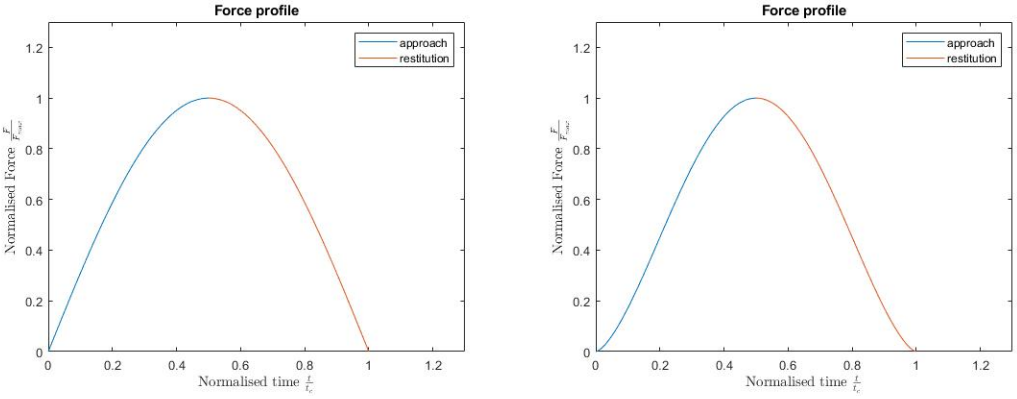

(a) Force profile according to eq. 1.2

(b) Force profile according to eq. 1.4

Figure 1.13: Force profiles according to the two models based on Hertz's theory

In real impacts however, the main simplifying assumption that appears most limiting in Hertz's theory is the pure elastic behaviour of the bodies, where in reality a certain degree of energy dissipation for plastic phenomena must be taken into account. A well-trodden method to easily factor in complicated dissipative mechanisms (such the ones related to plasticity, hysteresis etc.) is the use of the coefficient of restitution e, defined as the ratio between the relative velocities in approach and separation [13]:

$$e = \frac{v_1^+ - v_2^+}{v_1^- - v_2^-} \tag{1.6}$$

Where the superscript + refers to the instant after the collision, the superscript – refers to the instant before the collision, and v_1 and v_2 are the modulus of the velocities of the two bodies.

In the case of a fixed, stationary target 2 ($v_2^+ = v_2^- = 0$) and a moving impacting object 1 (like in pyroshock test impacts), the coefficient of restitution becomes:

$$e = \frac{v_1^+}{v_1^-} \tag{1.7}$$

The kinetic energy carried by 1 before the impact is:

$$E_k^- = \frac{1}{2} m_1 {v_1^-}^2 \tag{1.8}$$

while after the impact is:

$$E_k^+ = \frac{1}{2} m_1 {v_1^+}^2 \tag{1.9}$$

thus the dissipated energy is:

$$\Delta E_k = E_k^- - E_k^+ = \frac{1}{2} m_1 {v_1^-}^2 (1 - e^2) \tag{1.10}$$

It is possible to perform the same reasoning on the modulus of the momentum carried by 1 before the impact:

$$|p^-| = m_1 v_1^- \tag{1.11}$$

and after the impact

$$|p^+| = m_1 v_1^+ \tag{1.12}$$

thus the change in momentum of the body 1 is:

$$|\Delta p| = |p^-| + |p^+| = m_1 v_1^- (1 + e) \tag{1.13}$$

The momentum change during the collision is a fundamental quantity in the study [6], where it is used as an input for the parametric model for the SRS prediction.

In the study [14], which will be described in more detail later, the coefficient of restitution modifies the separation phase of the force pulse of a pure elastic collision modelled as a raised sine (Hann function), choosing the peak of the force as the separation point between the approach and separation phase.

The force profile is:

$$F(t) = \begin{cases} F(t) = F_{max} sin^2(\frac{\pi t}{\tau_i}) & 0 \le t \le t_{max} \\ F(t) = F_{max} sin^2(\frac{\pi t}{\tau_o} + \frac{\pi(\tau_o - \tau_i)}{2\tau_o}) & t_{max} < t \le t_c \end{cases} \tag{1.14}$$

Where τ_i is the period of the first half of the Hann function, τ_o is the period of the second half of the function and t_{max} is the time at which the force reaches its peak and happens the transition from the approach phase to the restitution phase.

The total contact time t_c is:

$$t_c = 2.9432 \left[\frac{15 m_1 (\frac{1-\nu_1^2}{E_1} + \frac{1-\nu_2^2}{E_2})}{16\sqrt{R_1 v_1^-}} \right]^{\frac{2}{5}} \tag{1.15}$$

The durations τ_i and τ_o are related by the coefficient of restitution that becomes, after the integration of the force pulse over time to calculate the momentum [14]:

$$e = \frac{v_1^+}{v_1^-} = \frac{\tau_o}{\tau_i} \tag{1.16}$$

In this model, the coefficient of restitution is calculated according to Zener's theory [15], that specifically describes the impact between a sphere and a plate:

$$e = exp\left(-1.7191 \frac{1}{4\sqrt{3}} \left(\frac{\pi\rho_1}{\rho_2}\right)^{\frac{3}{5}} \left(\frac{2R_1}{s}\right)^2 \left[\frac{{v_1^-}^{2}\rho_2(1-\nu_2^2)}{E_2}\right]^{\frac{1}{10}} \left[1 + \frac{E_2(1-\nu_1^2)}{E_1(1-\nu_2^2)}\right]^{-\frac{2}{5}} \right) \tag{1.17}$$

Where ρ is the density of the objects, R_1 is radius of the impacting one, ν_i and E_i are the Poisson's ratio and the Young's modulus.

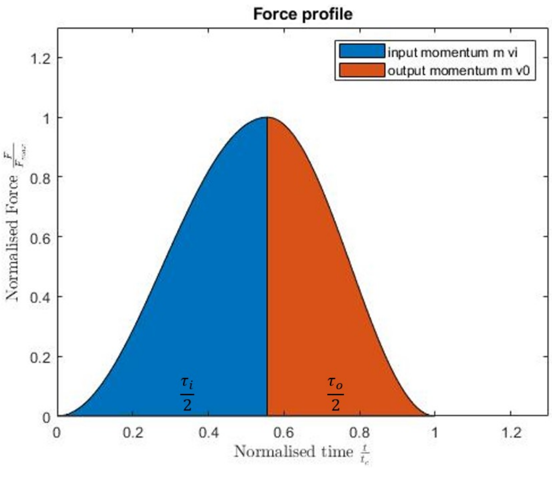

Figure 1.14: Momentums represented as areas (blue for input and red for output) and durations τ_o, τ_i

The last model present in the literature proposed in this work is the contact model proposed by Hunt and Crossley in [13], that can be adapted as in [16] to obtain:

$$F(t) = K\delta^n \left[1 + \frac{3(1-e)}{2}\frac{v_1}{v_1^-}\right] \tag{1.18}$$

Where

$$K = \frac{4}{3\left(\frac{1-\nu_1^2}{E_1} + \frac{1-\nu_2^2}{E_2}\right)}\sqrt{\frac{R_1 R_2}{R_1 + R_2}} \tag{1.19}$$

In the case of a sphere of radius R_1 impacting on a plate $R_2 \to \infty$

$$\lim_{R_2 \to \infty} K = \frac{4}{3\left(\frac{1-\nu_1^2}{E_1} + \frac{1-\nu_2^2}{E_2}\right)}\sqrt{R_1} \tag{1.20}$$

Note that this formulation requires the knowledge of the velocity and penetration of the bodies to compute the contact force; the position of the two colliding objects is usually measured by high-speed cameras, while in this study the dataset analysed only contains acceleration and force measurements. To overcome this limitation, a numerical integration was performed to obtain velocities and displacements data as will be further explained in Chapter 3.

1.5 Limitations of current approaches

All the standard test benches are tailored on a specific impact source and answer to the necessity of having a predictable and repeatable testing setup; however, having different impact sources on the same test bench open to the possibility of gathering different data to ultimately validate the model proposed in [6].

Regarding contact models, even if in [6] the use of the modified Hann function (1.14) gave satisfactory results, further studies can be made on the characterisation of the collision, especially with access to a test bench capable of collecting more data such the one that is currently being developed.

1.6 Improvements proposed

Due to safety concerns and feasibility, a mechanical excitation pyroshock test bench, consisting in a steel frame on which to hang the vertical resonant plate, was selected at the start of the project by the laboratory team; the design means of excitation are hammer impacts and projectile impacts, but further mechanical methods are possible.

This type of test bench offers a controlled, adaptable and repeatable way to simulate mid and far-field shock environments using different impact generating methods with commonly available laboratories equipment (hammers, projectiles etc.), without the additional risks of explosive devices.

The structure adopted will be further analysed in Chapter 2.

In the second part of this work, an analysis of contact characteristics was made on an available dataset of hammer impacts [14]. In particular, the work focused on comparing the experimental force profile with that provided by the above models.

Note that the object of this work is not to prove the validity of the many contact models proposed in the literature, but rather find a model that better interpolate the experimental data obtained by the acquisition campaign in [14].

Chapter 2

Frame design

This chapter will describe the analysis done on the test bench from the point of view of the design and structural verification, from the initial information and constraints to the final results.

2.1 Design constraints

The constraints for the dimensioning of the system were given by the laboratory available space; a specific area, long enough so that an air gun to hit the plate could be developed, was identified at the start of the project to house the test bench and the safety device.

A previously developed CAD model of the laboratory was used to virtually fit the structure and verify that no interference with the surrounding elements was present.

The maximum dimensions of the testbench and its accessories were determined as:

- Max height: 2900 mm
- Max length: 3600 mm
- Max width: 2000 mm

The possibility of having people behind the target plate without a solid separation wall induced the necessity to design a safety system, as it will be later discussed.

As a starting point, a plausible load case was assumed: the structure should had been able to sustain a plate of steel of a mass up to 1000 kg hanged on two points, and was required to be assembled on site due to low accessibility of the laboratory.

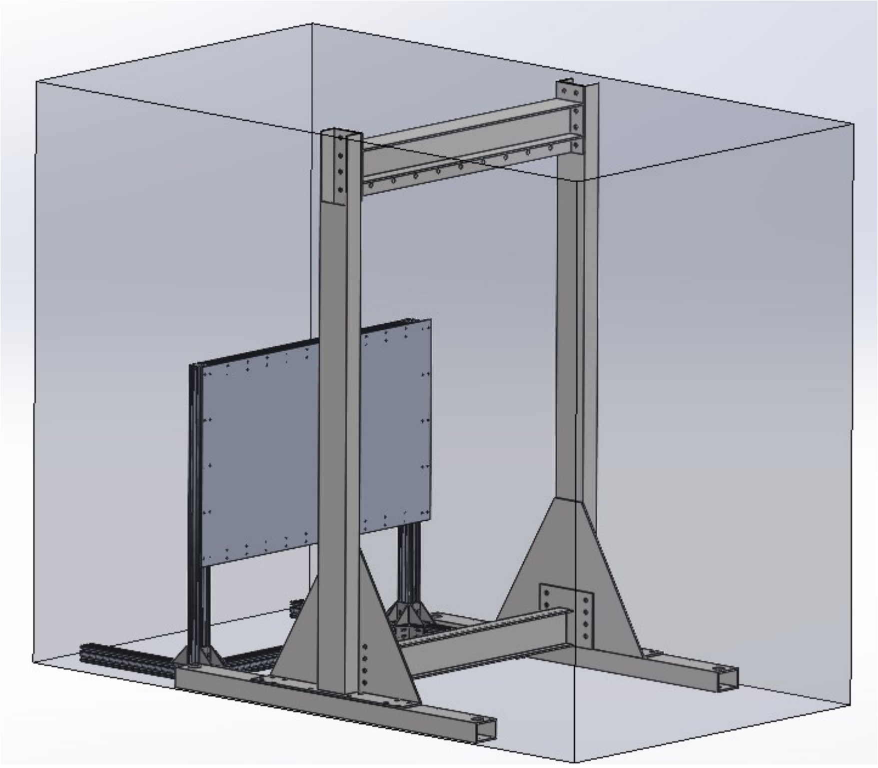

Figure 2.1: Frame and safety system inside the maximum dimensions

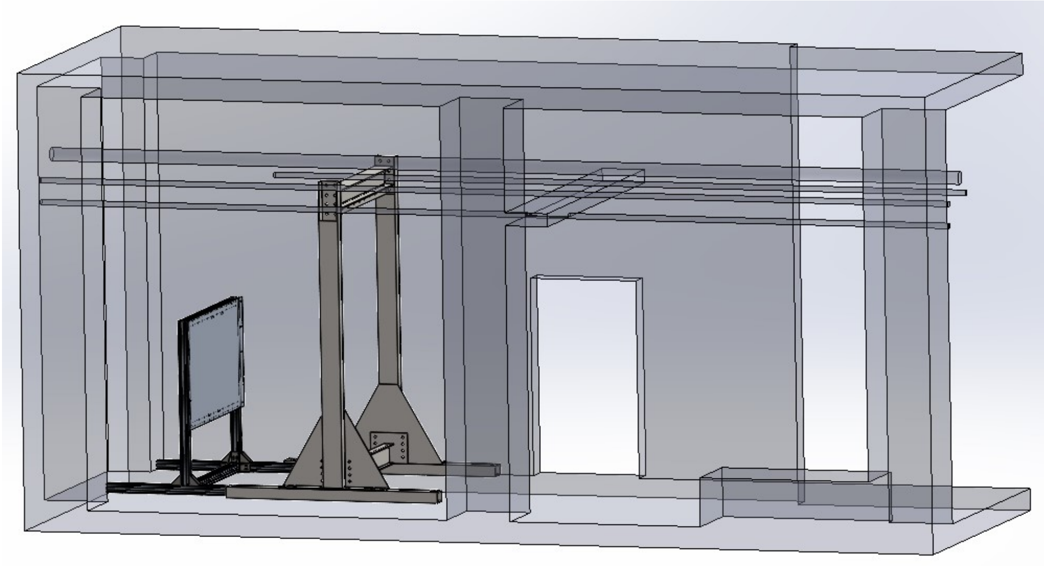

Figure 2.2: Laboratory mockup

2.2 Design choices

The geometry selected by the laboratory researchers was oriented towards a H-frame made with steel profiles to support the resonant plate, designed to be hit perpendicular to the plane. This configuration allows for a variety of impacting methods (hammer impact, powder actuated tool, compressed air-lunched bullets, etc.) and different resonant plate materials and configurations (fixed or free boundary conditions), making it a good choice for an experimental test bench that can be modified in the future.

The dimensions allow the installation of plates up to 1.5 meters of width and 2 meters of length, and allows suspended installation using chains, ropes or springs depending on the desired boundary conditions.

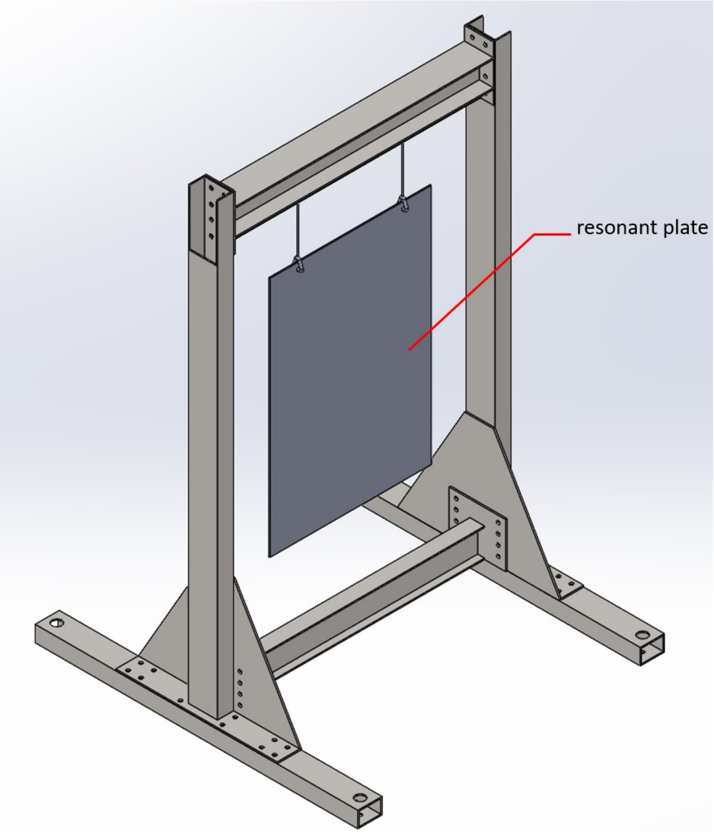

Figure 2.3: Test bench CAD

The study started from an already developed project, in which the geometry, loads and connectors had been selected to fit the heaviest conceivable use of the system. Bolted and welded structural steel profiles, usually used in carpentry, were used for the frame construction.

The objective of this study was to verify and double-check a part of the static structural calculations required to ensure the correct functioning of the structure.

2.3 Global analysis

The geometry of the structure provided as a starting point of the project was translated into the frame model as in figure 2.4b to perform the calculations:

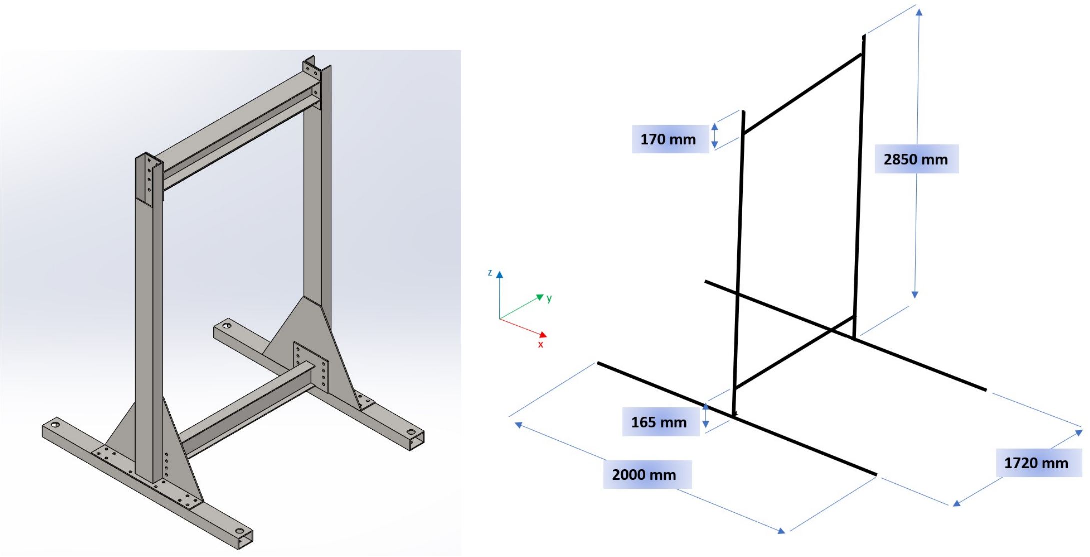

(a) (b)

Figure 2.4: CAD of the frame and model

The loads assumed by previous analysis were applied as in figure 2.5

P1	P2	F1	F2
15000 N	15000 N	1500 N	1500 N

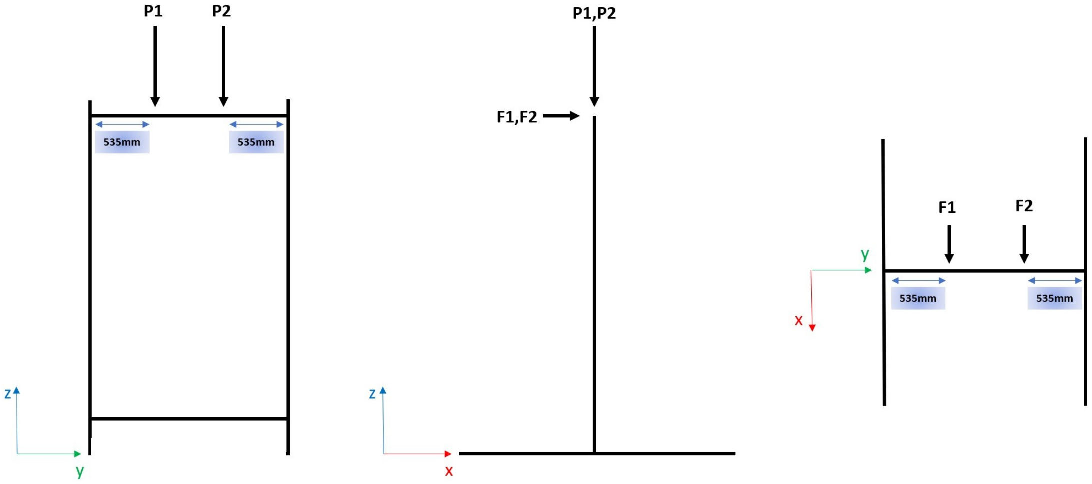

Figure 2.5: Position of the loads applied

The finite element analysis performed to evaluate the stress distribution in the structure under the load case of figure 2.5 was carried out using Simulation, a FEM software integrated in SolidWorks.

All the steps necessary for the setup of the analysis were:

- Bolted connections: as a first choice, M20 grade 8.8 bolts were selected as connection items; the software required to insert the preload applied to the bolt, that had been determined following the European standard EN 1993-1-8 Section 3.6.1 [17] as:

  $$F_{p,Cd} = 0.7\ f_{ub}\ \frac{A_s}{\gamma_{M7}} \tag{2.1}$$

  Where $F_{p,Cd}$ is the preload, f_{ub} is the bolt ultimate tensile strength, A_s the bolt effective area and γ_{M7} a safety coefficient (suggested by [17]). The resulting values were:

f_{ub}	A_s	γ_{M7}	$F_{p,Cd}$
800 MPa	$245\,mm^2$	1.1	$124727\,N$

- Constraints: the constraint imposed was the fixed geometry of the inferior faces of the structure to simulate the approximately rigid connection with the ground (figure 2.6a).

- Materials: the steel used was a structural steel (S355) with a yield strength of 355 MPa and an ultimate tensile strength of 510 MPa.

- Loading conditions: the loads values, positions and directions were applied as in figure 2.5, while the points of applications were the two holes where the chains had to be hooked to support the resonant plate (figure 2.6b).

- Local interactions: surface-to-surface, non-penetration contact between each component.

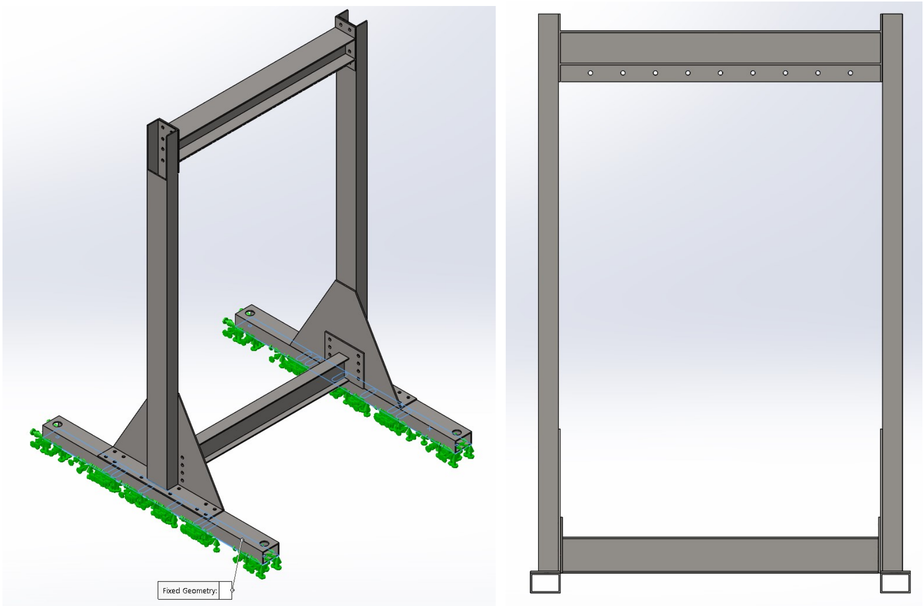

(a) Position of the fixed geometry contraint **(b)** Front view in which the holes in the top beam to which connect the plate are visible

Figure 2.6: CAD images of the frame

2.3.1 Results

Stress values were well below the yield limit of the material (355 MPa) throughout the whole structure, with the 65 % of the whole volume subjected to less than 10 MPa (and a safety coefficient of 35.5) (figure 2.7a) and only 3% of the volume of the structure subjected to more than 100 MPa (figure 2.7b), concentrated in the bolted connections area, where the high preload applied generated plastic deformations only on the boundaries of the holes, but still lower than the ultimate tensile strength of the material (495 MPa of maximum equivalent stress experienced against an ultimate tensile strength of 510 MPa) (figure 2.8). Further discussions were made on chapter 2.2.2

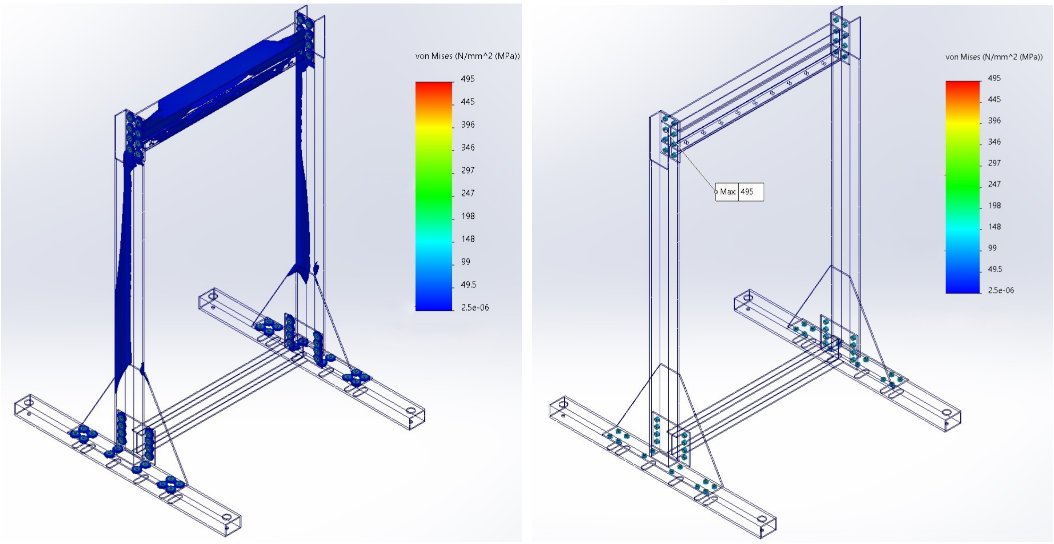

(a) Stress higher than 10 MPa **(b)** Stress higher than 100 MPa

Figure 2.7: Von Mises stress result

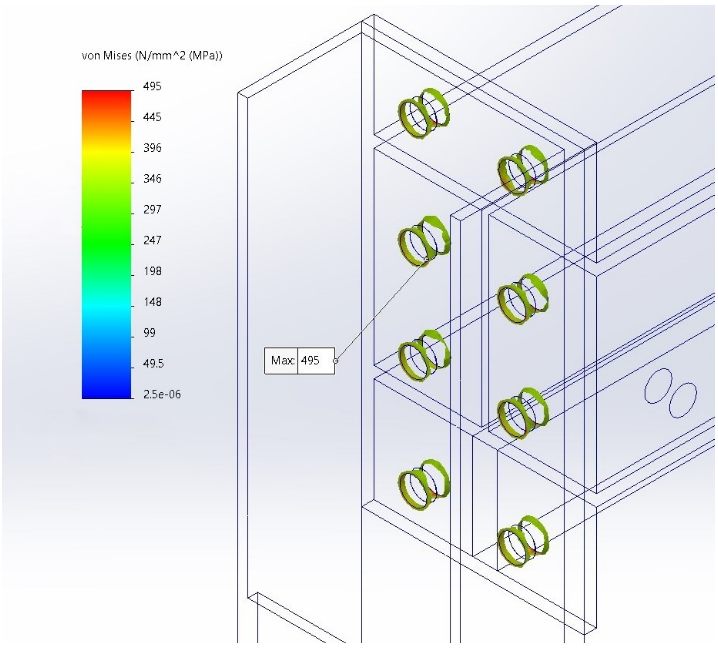

Figure 2.8: Stress result on bolted connections: stress higher than 355 MPa (yielding point)

2.4 Components analysis

After the analysis of the global behaviour of the structure under the static loads, some further calculations were carried out following technical standards to check the correct dimensioning of particular elements, such as welds and bolted connections. Two main components were analysed singularly:

- Top welded bar, whose task is to connect the chains to the main structure.
- Bolted connection of the superior beam with the columns.

2.4.1 Weld resistance

The component analysed in detail regarding the welding resistance was the connection bar on the top of the structure, used to connect the resonant plate and the structure with chains or other devices depending on the desired boundary conditions.

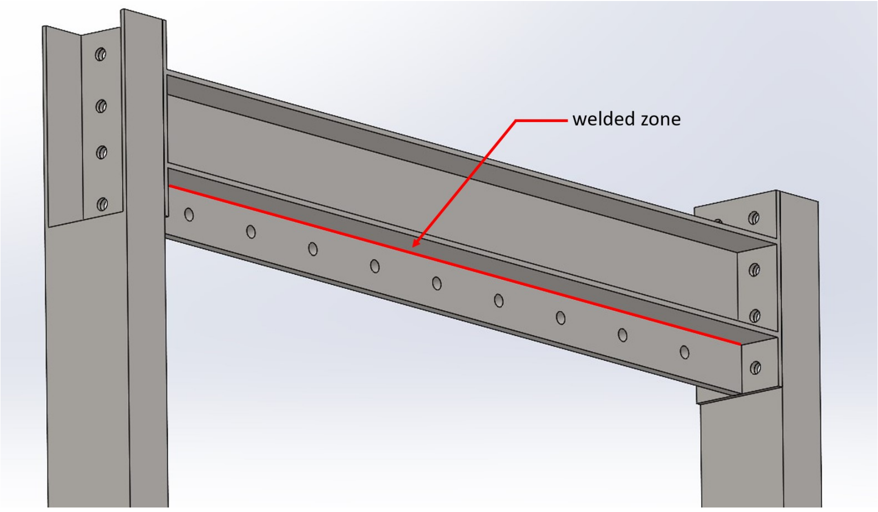

Figure 2.9: Particular of the structure: top bar welded zone

To perform the calculations, three main assumptions were made:

- The total weld length was assumed, as a first hypothesis, to be 50 % the total length of the bar, in order to not deform the structure with possible induced residual stress.
- The total load was considered vertical (ignored the 6° angle that existed due to the x and y components of the loads), of module $P_{tot} = \sqrt{(2P)^2 + (2F)^2}$ and uniformly distributed on the weld length.
- The weld calculations were performed on a tee joint model with an assumed throat thickness of 3 mm (the minimum value recommended by [17]).

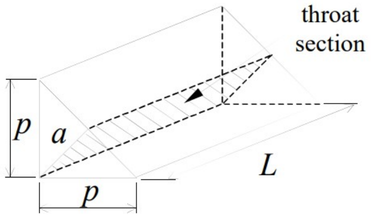

(a)

Total length of the component	$1600\,mm$
Weld length l	$800\,mm$
Throat thickness a	$3\,mm$
Foot of the weldline p	$800\,mm$
Effective weld length $L = l - 2a$	$794\,mm$
Throat area $A_{res} = L \cdot a$	$2382\,mm^2$

Figure 2.10: Tee joint straight fillet

According to EN1993-1-8, the resistance of the weld was assessed following the directional method, in which the stress components are computed on the throat section; the two checks to be performed were:

- $\sqrt{(\sigma^g{}_\perp)^2 + 3(\tau^g{}_\perp{}^2 + \tau^g{}_\parallel)^2} \leq \frac{f_u}{\beta_w \gamma_{M2}}$
- $\sigma^g{}_\perp \leq \frac{0.9 f_u}{\gamma_{M2}}$

Where $\sigma^g_\perp$ is the normal stress perpendicular to the throat, $\tau^g_\perp$ is the shear stress (in the plane of the throat) perpendicular to the axis of the weld, $\tau^g_\parallel$ is the shear stress (in the plane of the throat) parallel to the axis of the weld.

f_u is the ultimate tensile strength of the parts joined, β_w is the correlation factor depending on the steel grades (for S355, f_u = 510 MPa $\beta_w = 0.9$). The safety coefficient recommended by [17] is $\gamma_{M2} = 1.25$

The resulting stress components were calculated as:

$$\sigma^g{}_\perp = \tau^g{}_\perp = \frac{\sqrt{2} P_{tot}}{4} \frac{1}{A_{res}} \qquad \tau^g{}_\parallel = 0 MPa \tag{2.2}$$

The results of the structural verification were:

- $\sqrt{(\sigma^g{}_\perp)^2 + 3(\tau^g{}_\perp{}^2 + \tau^g{}_\parallel{}^2)} \leq \frac{f_u}{\beta_w \gamma_{M2}} \quad \rightarrow \quad 9\,MPa \leq 453\,MPa \quad \rightarrow$ verified
- $\sigma^g{}_\perp \leq \frac{0.9 f_u}{\gamma_{M2}} \quad \rightarrow \quad 4.5\,MPa \leq 367\,MPa \quad \rightarrow$ verified

Since both of the requirements of [17] were met, the weld was considered to be verified.

2.4.2 Bolted connections

The exact analytical calculations of the transmitted forces and moments through the joints was made complex by the geometry of the connections and the difference in section of the columns, that made difficult to determine the rotational stiffness of the connections. A simple but still conservative way to verify the bolted connections had been the assumption of ideal fixed connections, as in figures 2.11

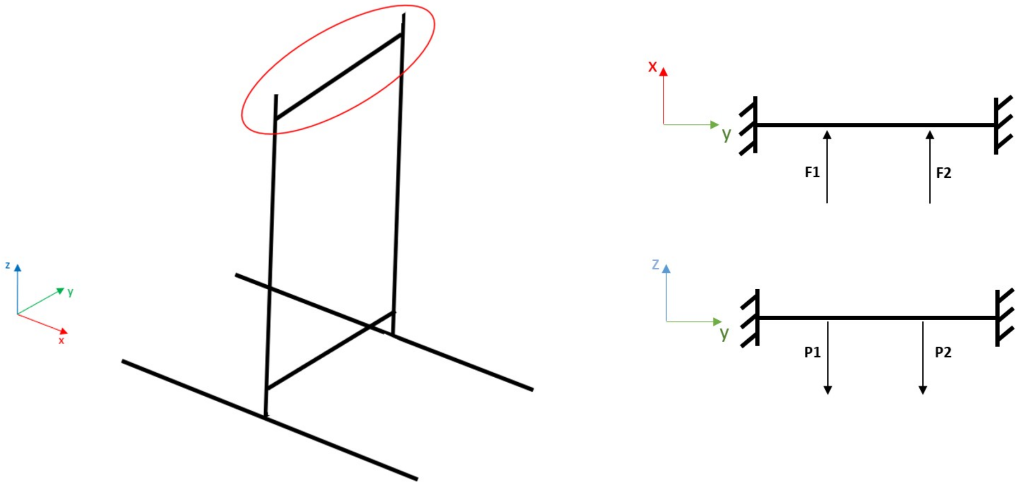

Figure 2.11: Top bar modelled as a beam fixed at both ends

The values of forces and moments on the hyperstatic structure were retrieved from structural engineering manuals [18]. Performing the calculations for both the vertical and horizontal forces, the results on the bolted plate on the top beam were as in figure 2.12

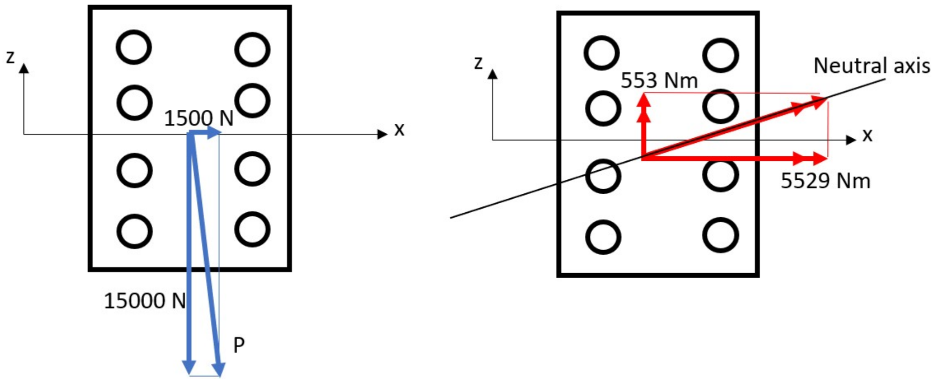

Figure 2.12: Forces and moments on the top beam bolted plate

The first step consisted in the calculations of the tension and shear forces on the bolts. The position of the neutral axis was necessary to determine the maximum tension force on the most stressed bolt (top-left one); for simplicity and still keeping the most conservative approach, the position of the neutral axis was taken in the centre of the connection, parallel to the x axis (figure 2.13).

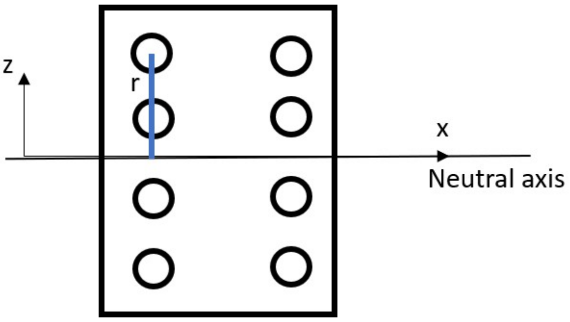

Figure 2.13: Simplified position of the neutral axis

From geometric analysis, the distance between the analysed bolt and the neutral axis was $r = 130\, mm$ and the moment of area around the neutral axis of the plate was $I = 5.896 * 10^8\, mm^4$ (data derived from Solidworks CAD model).

The tension stress on the analysed bolt was then calculated as:

$$\sigma_t = \frac{M_{tot}}{I} r = \frac{\sqrt{5529^2 + 553^2} \cdot 10^3}{5.896 \cdot 10^8} \cdot 130 = 1.23\ MPa \tag{2.3}$$

On the bolt, the total traction force due to the moments was $F_t = \sigma_t A_t$, to which was added the tension of the preload applied to the M20 bolt, as determined in equation 2.1.

As a result, the total tension force on the most heavily loaded bolt was:

$$F_{t,Ed} = \sigma_t A_s + F_{p,Cd} = 125\, kN \tag{2.4}$$

The total shear force on the bolt $F_{v,Ed}$ (component parallel to the plane of the connection) was calculated as the vectorial sum of two components:

1. The shear force, that was the planar force P applied to the connection divided by 2 (one per side of the connection), resulting in: $V = \frac{P}{2} = 7537\, N$ and for the single bolt: $V_b = \frac{V}{4} = 1884\, N$
2. The force resulting from the torque $T = V\, d$, where d was the distance between the bolt and the neutral axis for torque ($d = 40\, mm$); the resulting force on the single bolt was calculated as $V_t = \frac{T\ r}{\sum {r_i}^2}$ where r was the distance between the bolts and the neutral axis.

   As a result: $V_t = \frac{7537 \cdot 40 \cdot 130}{(40^2 + 40^2 + 130^2 + 130^2)} = 1059\ N$

The total resulting shear force on the bolt was:

$$F_{v,Ed} = \sqrt{{V_t}^2 + {V_b}^2} = 2161\ N \tag{2.5}$$

After the determination of the forces acting on the most loaded bolt, three different checks were carried out according to [17]: slip resistance of the connection, tension-shear resistance of the bolts and bearing resistance of the bolt holes.

- Slip-resistant connection subjected to shear and tension: the shear force was compared to the shear resistance of a single bolt, calculated according to [17] as:

  $$F_{s,Rd} = \frac{k_s n \mu F_{p,C}}{\gamma_{M3}} \tag{2.6}$$

  Where: $F_{s,Rd}$ is the slip resistant force, $n = 1$, $k_s = 1$, $\gamma_{M3} = 1.25$, μ is the friction coefficient (conservative choice $\mu = 0.2$), $F_{p,C}$ is the preload applied. The total shear force $F_{v,Ed}$ must be lower than $F_{s,Rd}$ to ensure no-slip condition:

  $$F_{v,Ed} \ \leq F_{s,Rd} \rightarrow 2161\,N \leq 19956\,N \rightarrow verified \tag{2.7}$$

- Tension-shear: the bolt must be able to sustain the combined loading condition:

  $$\frac{F_{v,Ed}}{F_{v,Rd}} + \frac{F_{t,Ed}}{1.4 F_{t,Rd}} \leq 1 \tag{2.8}$$

  Where the resistance values (relatively for shear and tension) were calculated as: $F_{v,Rd} = \frac{\alpha_v f_{ub} A_s}{\gamma_{M2}}$ (where $\alpha_v = 0.6$ for 8.8 class) $F_{t,Rd} = \frac{k_2 f_{ub} A_s}{\gamma_{M2}}$ (where $k_2 = 0.9$).

  As a result:

  $$\frac{2161\,N}{94080\,N} + \frac{125\,kN}{1.4 \cdot 141120\,N} = 0.66 \leq 1 \rightarrow verified \tag{2.9}$$

- Bearing resistance: the resistance of the connection against bearing pressure, a contact phenomenon between the screw and the hole that can induce plastic deformation in the contact region, that was verified as:

  $$F_{v,Ed} \leq F_{b,Rd} \tag{2.10}$$

  Where the bearing resistance was calculated as:

  $$F_{b,Rd} = \frac{k_1 \alpha_b f_u d\ t}{\gamma_{M2}} \tag{2.11}$$

  Where d is the bolt diameter, t is the thickness of the plate, f_u the ultimate strength of the plate, and α_b and k_1 are parameters that depends on the geometry of the connection. As a result:

  $$2161\,N \leq 98.9\,kN \rightarrow verified \tag{2.12}$$

2.5 Safety system

The possibility of using a projectile to impact the plate required the addition of a safety measurement in order to avoid accidents; in particular, a barrier was designed to keep the area behind the test bench and in line with the bullet trajectory safe even in the event of an unintentional shot without the target plate installed.

The dimensioning started from the following constraints:

- Height of the trajectory: max 1.5 meter from the ground
- Load applied to the structure: equal to the total horizontal load on the test bench frame ($F = F_1 + F_2 = 3000\,N$)
- Dissipation mechanism: plastic deformation of an aluminum plate

Due to the last constraint, the barrier was designed to be fixed on the ground, possibly using the same anchorage system of the test bench frame (dowels), leaving no room for other dissipation mechanisms involving dynamic effects.

The first design choice was the use of standard extruded aluminum profiles for the frame, due to the low cost, modularity and availability.

The components, assembled with standard connectors, were arranged as in figure 2.14a

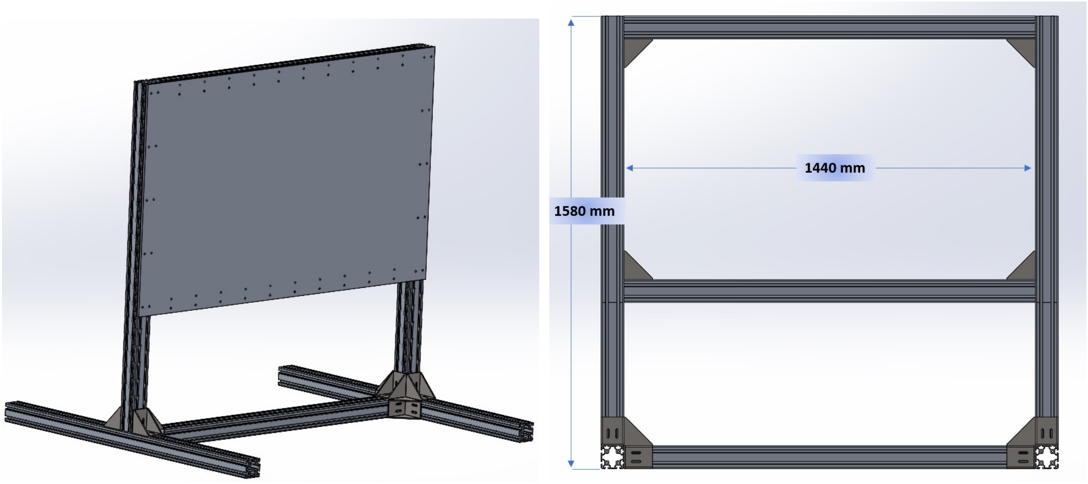

(a) **(b)**

Figure 2.14: CAD of the safety system and frontal dimensions

The aluminum plate was designed to be fixed along the profile through bolts and t-slot nuts on the frame. The frontal footprint of the plate was selected by assuming the dimensions of the area that can be affected by the bullet trajectory, choosing a plate of 1000mm of height and 1440mm of length; the selection of the thickness was made in order to guarantee that during the impact, the plate should not be perforated by the projectile.

To guarantee that constraint, the velocity at which the projectile perforate the plate was calculated following ballistic studies as [19].

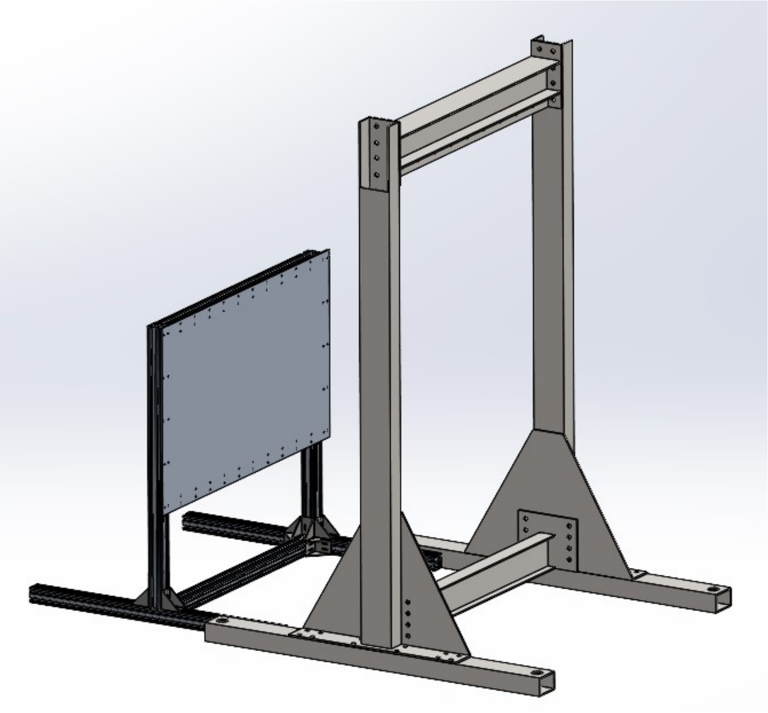

Figure 2.15: Disposition of the safety system and the test bench

In particular, the article [19] estimates the minimum perforation velocity V_{xn} of a projectile impacting perpendicularly on a thin plate (thickness lower than half the length and the diameter of the projectile) as:

$$V_{xn} = \frac{8\tau T^2}{\rho C d L}\left[1 + \sqrt{1 + \frac{L}{T} + \frac{\rho C^2 d(L+T)}{16\tau T^2}}\right] \tag{2.13}$$

Where τ is the dynamic shear strength of the plate, ρ is the mass density $(\frac{mass}{gravity\,acc.})$ of the plate, C is the sonic velocity ($\sim 343\,m/s$), d is the projectile diameter, T is the plate thickness and L is the projectile length (note that equation 2.13 requires that all the dimensions are expressed in Imperial System Units).

Under the assumption of an aluminum projectile of 50 mm of diameter, 200 mm length, and the hypothesis, according to [19], that the dynamic shear strength is approximately two times the static shear strength, for an aluminum 7075 ($\tau = 660$ MPa) plate of thickness $T = 10\,mm$ the minimum perforation velocity resulting was $337\,m/s$, assuring a good safety margin to an expected impacting velocity of $80\,m/s$.

In case of impact, the metallic plate should be at least visually inspected and substituted if plastic deformation are encountered.

The limitation of the study [19] that could mostly affect the result calculated was the required similarity between the hardness of the impacting bullet and the plate: in case of use of a steel tip on the aluminium bullet, the hardness difference between the two colliding materials could invalidate the model's assumptions and lead to inaccurate results.

Further analysis, or even a test campaign on a series of plates with different thickness and different bullet tips could be implemented in the future.

To check for the structural integrity of the frame, a static FEM analysis was performed using Simulation (Solidworks).

All the steps necessary for the setup of the analysis were:

- Constraints: the constraint imposed was the fixed geometry of the inferior faces of the aluminum profiles to simulate the approximately rigid connection with the ground.
- Materials: the aluminum used for the extruded profiles was a 6063-T5 with a yield strength of 145 MPa and an ultimate tensile strength of 186 MPa, while for the connectors the steel used was an AISI 304 with a yield strength of 215 MPa and an ultimate tensile strength of 505 MPa.
- Loading conditions: the load applied was the total horizontal force $F = 3000\,N$, uniformly distributed on the contact surface between the plate and the structure, as in figure 2.16.
- Local interactions: bonded components.

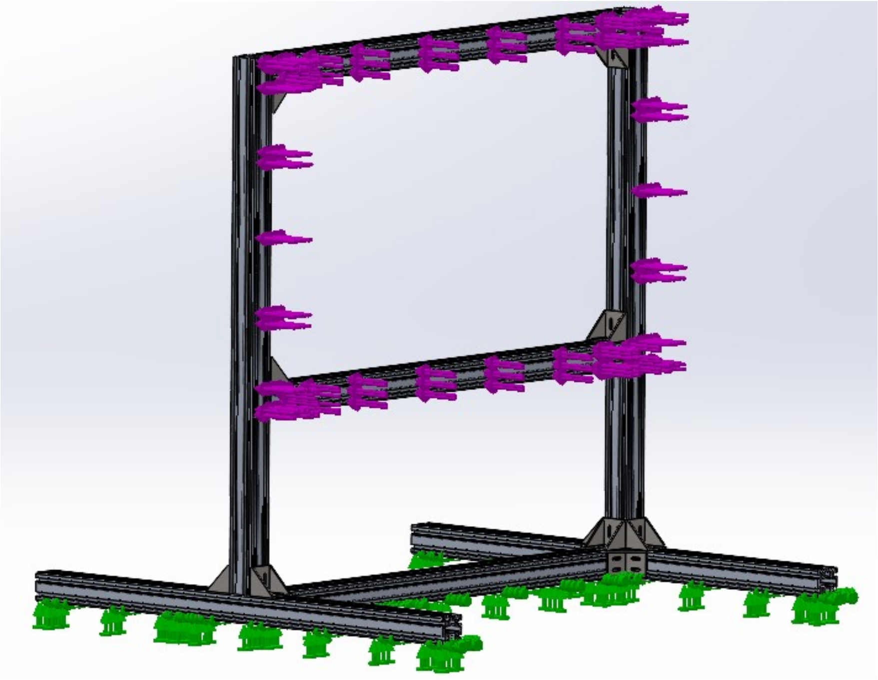

Figure 2.16: Loads (purple arrows) and contraints position (green arrows) on the frame

The result of the simulation showed an acceptable stress distribution, with the maximum equivalent stress (Von Mises) of 118 MPa, located on the lower intersection between the column and the base of the frame, that lead to a minimum safety coefficient against plastic deformation for the structural integrity of the frame of 1.23

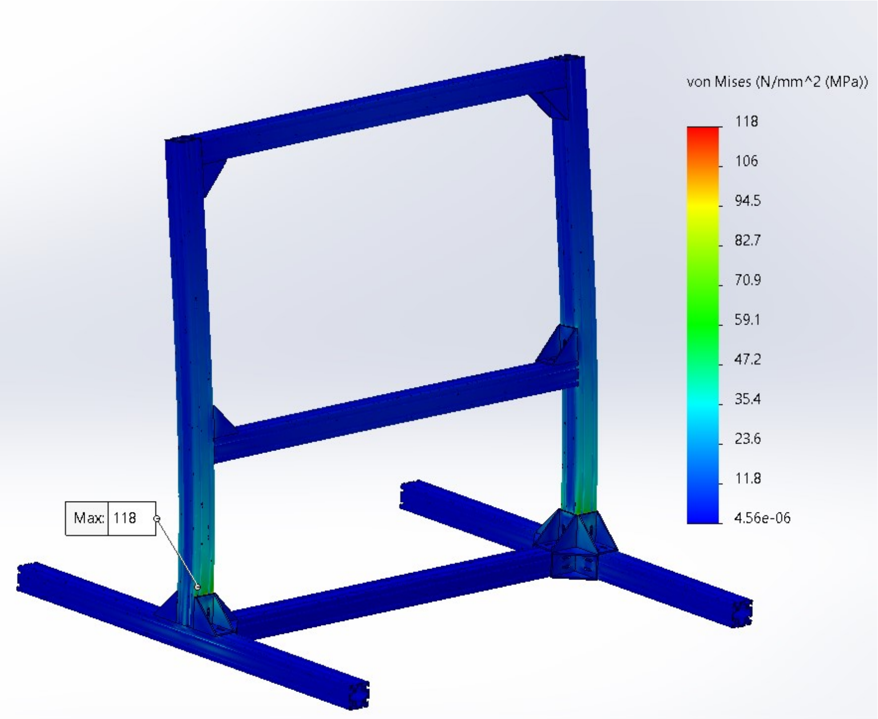

Figure 2.17: Von Mises stress result

Chapter 3

Contact analysis

In this study, to gain insight on the characteristics of the impulse generated, its profile during an impact and accurately simulate the input momentum in the model proposed in [6], an already structured database of hammer-plate impacts was exploited [14].

3.1 Reference dataset

The dataset contains 1800 hammer-plate impacts (10 repeated impacts for 180 different tests configurations) and has already been deeply analysed in [14], where all additional information can be retrieved.

In this work, only a brief introduction to the dataset is given.

The following parameters had been considered:

Factor	Low Level	Medium Level	High Level
Impact position	#1	#2	#3
Hammer speed	Low	-	High
Hammer head material	Aluminum	Delrin	Polyurethane
Anvil plate material	None	Aluminum	Steel
Anvil insulator	None	-	Polymeric
Plate boundary conditions	Free	-	Fixed

In each test, 10 hammer impacts on a plate were performed, spaced by approximately 6 seconds each. The test methodology was a full factorials Design of Experiment (DOE), a method that takes into account not only for the influence of each parameter, but also for the combination of the parameters. The total number of tests performed derives from the number of factors as in the table, where to each parameter 2 or 3 values (low-level, mid-level and high level) were assigned.

The data available were the accelerations recorded by 7 accelerometers on the plate, one on the hammer and a dynamometer on the hammer.

3.2 Data processing

The dataset provided an already structured MATLAB database with time-synchronised force and acceleration signals; the MATLAB code proposed in this study aimed at extracting the following features from the force signal acquired by the dynamometer and the acceleration signal acquired by the accelerometer positioned on the hammer tip:

- force peak value and time instant t_{max}
- instant of time in which the contact starts t_l
- instant of time in which the contact ends t_r
- acceleration profile during contact

From those data, it was possible to derive:

- total duration of the impact ($t_c = t_r - t_l$)
- duration of the approach and restitution phases ($t_{max} - t_l$ and $t_r - t_{max}$, respectively)
- velocity and displacement profile (numerical integrations of the acceleration profile)
- momentum of the approach and restitution phases
- coefficient of restitution

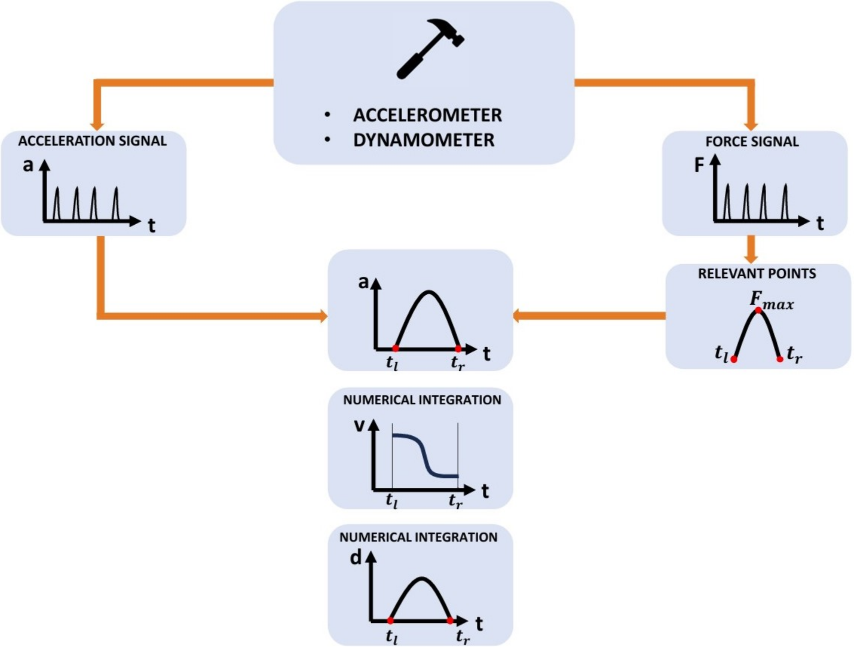

Figure 3.1: Data processing flow

Source	Data
Dynamometer	F_{max} t_l, t_r, t_{max} $e = \frac{mv_o}{mv_i}$ $e = \frac{\tau_o}{\tau_i}$
Accelerometer	acceleration $a(t)$ velocity $v(t)$ displacement $d(t)$ $e = \frac{v_o}{v_i}$

The extraction method was based on the hypothesis that the force profile (in accordance with theoretical models [12]) has a shape similar to a sine or raised sine wave; thanks to this assumption and to the known test procedure (one impact approximately every 6 seconds, for a total of 10 impacts), it was possible to find the instant of maximum force of the wave profile by resorting to the MATLAB function *findpeaks*, that gave as a result the location of the peak and its value.

The signal presented some noise and errors in the instants following the impact (negative force signal, thus due to an apparent but physically implausible state of traction on the hammer head 3.2 a) that let the method described prone to errors in the exact identification of the precise instants in which the force profile of the impact starts and finishes.

The force signal had therefore been manipulated to circumvent the inconvenience by selecting an appropriate percentage of the maximum force of each impact as the threshold level under which the signal is considered to end.

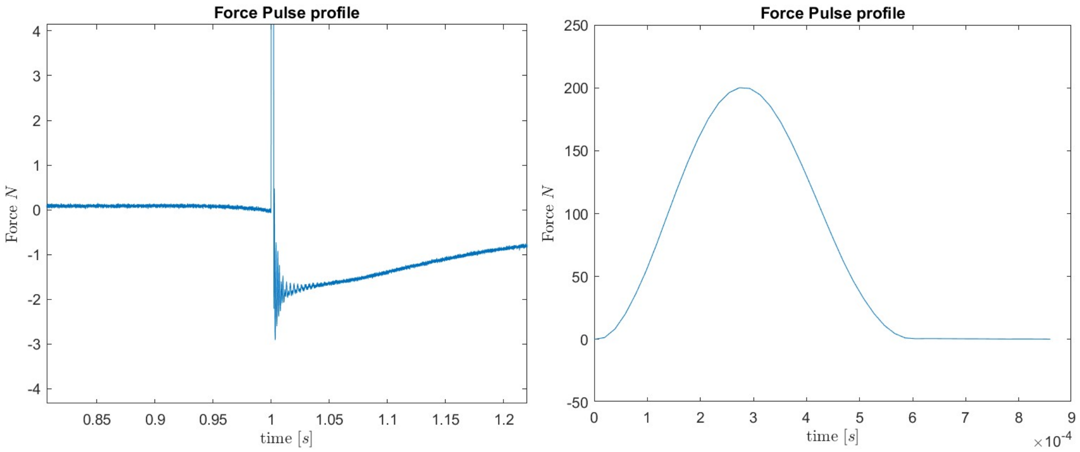

(a) Example of the noise in the force signal **(b)** Error in contact duration due to low threshold

Figure 3.2: Noise and error in the features extraction process

In order to make a reasonable estimate of the threshold to be adopted, it was used the following rationale:

- The shape of the force profile of the impact pulse was approximated by a raised sine function
- The threshold value was expressed as a fraction x $(0 < x < 1)$ of the maximum force of each impact F_{max} : threshold value $= x\,F_{max}$
- The systematic error on the time estimation was calculated as the sum of the errors made on the left and right sides of the curve (approach and restitution), where t_l and t_r were the values identified by the thresholding method and t_l^* and t_r^* were the theoretical values of start and end of contact.

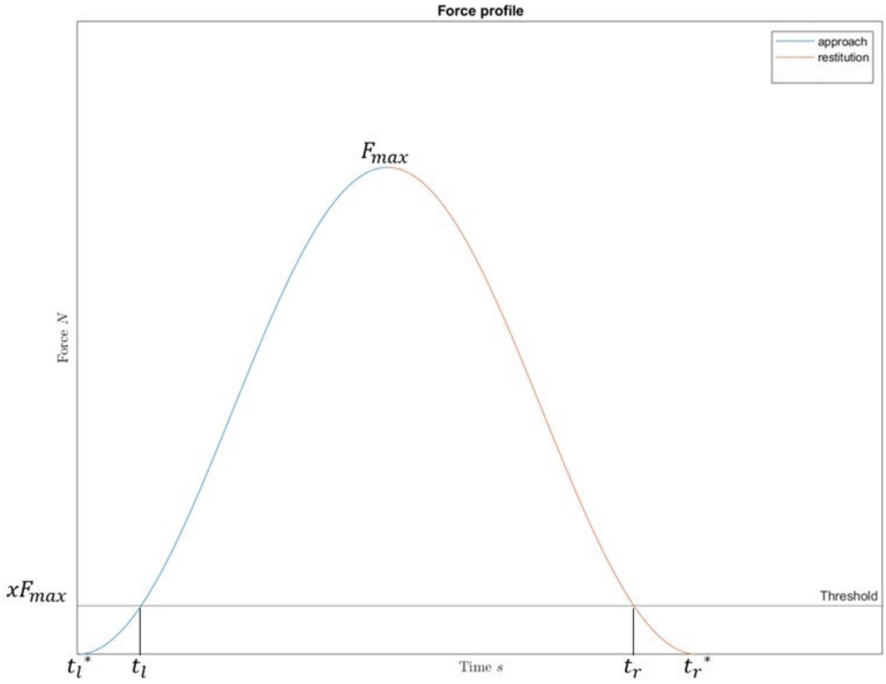

Figure 3.3: Thresholding method applied on a raised sine curve

Translating into equations:

$$\begin{cases} x\,F_{max} = F_{max} sin^2(\frac{\pi t_l}{t_c}) & 0 \leq t_l \leq t_{max} \\ x\,F_{max} = F_{max} sin^2(\frac{\pi t_r}{t_c}) & t_{max} < t_r \leq t_c \end{cases} \tag{3.1}$$

That yielded the result:

$$t_l = \frac{t_c}{\pi} \sin^{-1}\left(\sqrt{x}\right) \qquad t_r = \frac{t_c}{\pi} \sin^{-1}\left(-\sqrt{x}\right) + t_c \tag{3.2}$$

While the theoretical exact values of start and end of contact were $t_l^* = 0$ and $t_r^* = t_c$.

The systematic error was calculated as:

$$err = \frac{|(t_r - t_l) - ({t_r}^* - {t_l}^*)|}{{t_r}^* - {t_l}^*} = \frac{|t_c - \frac{2t_c}{\pi}\sin^{-1}(\sqrt{x}) - t_c|}{t_c} = \frac{2}{\pi}\sin^{-1}\left(\sqrt{x}\right) \tag{3.3}$$

As it can be seen, the threshold x is proportional as equation 3.3 to the error made on the estimation of the duration of the impact.

After a series of iterations with different values of x to detect potential errors in the extraction (a threshold set too low can lead to confusion between noise and signal, as can be seen in figure 3.2b), the threshold selected was $x = 0.003$ (0.3% of the maximum force), that generated an error on the impact duration of $err = 0.035$ (3.5% error), considered acceptable.

Note that this value can be easily modified on the code for the features extraction if further investigations make it necessary.

Once the time instants of start and end of contact had been identified on the force profile, analogous points (start and end of contact) were easily extracted from the accelerometer channel thanks to the time synchronization of the different acquisition channels.

From the acceleration profile of the pulse, it was possible to calculate the velocity and displacement of the hammer tip with a numerical integration of the data over the known contact time (figure 3.5 c-d).

To obtain the momentum of the impacting object and the momentum in the restitution phase, the area under the respective portions of the force profile (see figure 1.14) was calculated through numerical integration.

$$mv_i = \int_0^{t_{max}} F(t)dt \qquad mv_o = \int_{t_{max}}^{t_c} F(t)dt \tag{3.4}$$

All the 1800 impacts were analysed using this method; as it can be seen in figure 3.4a, the difference in force amplitude and contact duration for the different tests is large. If normalised for time of contact and maximum force, the profiles looks more similar (figure 3.4b).

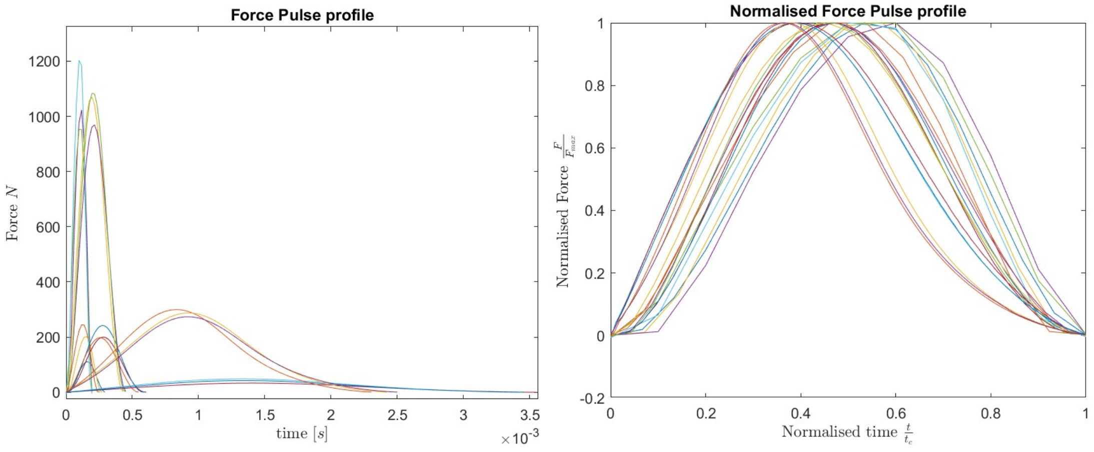

(a) **(b)**

Figure 3.4: Force pulse of the first impact (of 10) of the first 18 tests (of 180)

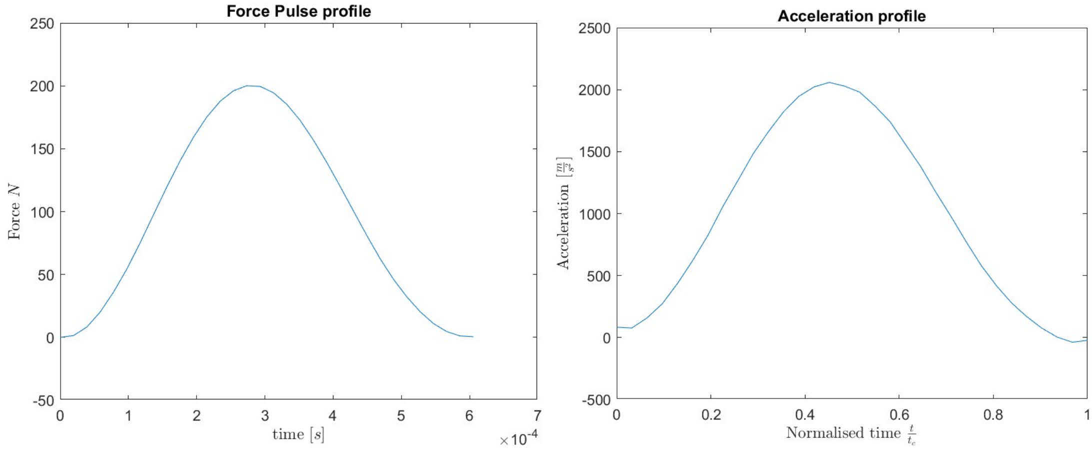

(a) Force pulse profile (from dynamometer) **(b)** Acceleration profile (from accelerometer, time normalised and opposite sign)

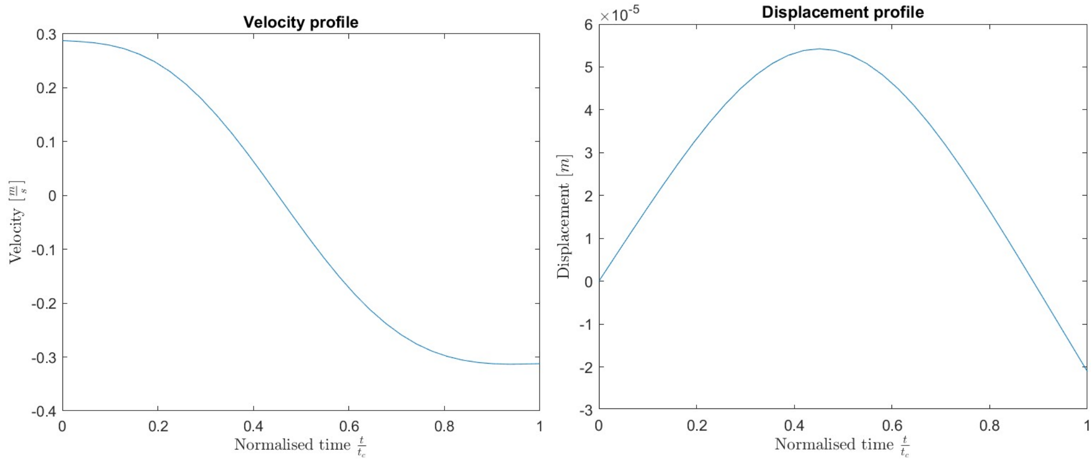

(c) Velocity profile (time normalised) **(d)** Displacement profile (time normalised)

Figure 3.5: Data obtained on a randomly selected test

Finally, the coefficient of restitution of the impacts was calculated using different definitions and sources:

- $e = \frac{v_o}{v_i}$ as standard literature definition, obtained from the integration of the accelerometer signal;
- $e = \frac{\tau_o}{\tau_i}$ as the definition that results from the model proposed in [14];
- $e = \frac{mv_o}{mv_i} = \frac{p_o}{p_i}$ that defines the coefficient of restitution as the ratio between the momentum in the approaching phase and the restitution one, obtained from the dynamometer features extraction.

As it can be seen in figure 3.6, all the methods show frequently a coefficient of restitution higher than 1, which is physically unacceptable for a collision without internal generation of energy. The problem has emerged also in [14], where the possible causes proposed were the sampling frequency (51.2 kHz to measure an average contact time of $10^{-4}\ s$) and the operator influence during the test.

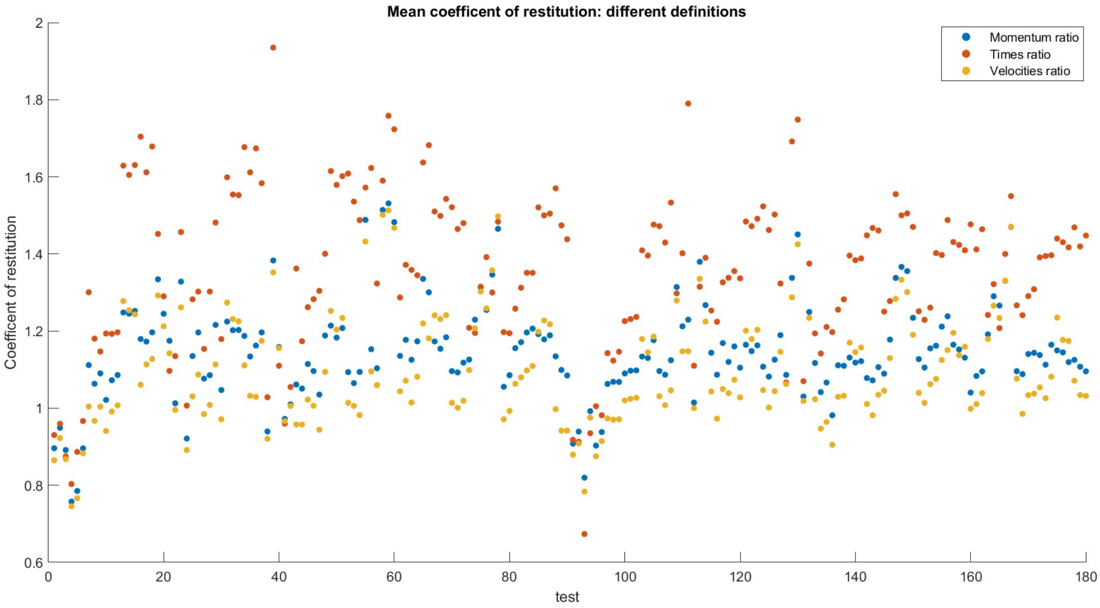

Figure 3.6: Mean coefficient of restitution of the 10 impacts over the 180 tests, using the three different definitions and different sources (velocity ratio from accelerometer, momentum ratio and time ratio from dynamometer)

Theoretically the definitions $e = \frac{v_o}{v_i}$ and $e = \frac{mv_o}{mv_i} = \frac{p_o}{p_i}$ are identical (constant mass), but due to the nature of the method used to calculate the momentum values (numerical integration over a force profile) and the velocity values (numerical integration of an acceleration obtained from a different sensor), the comparison between the two values was used to check the quality of the features extraction method proposed.

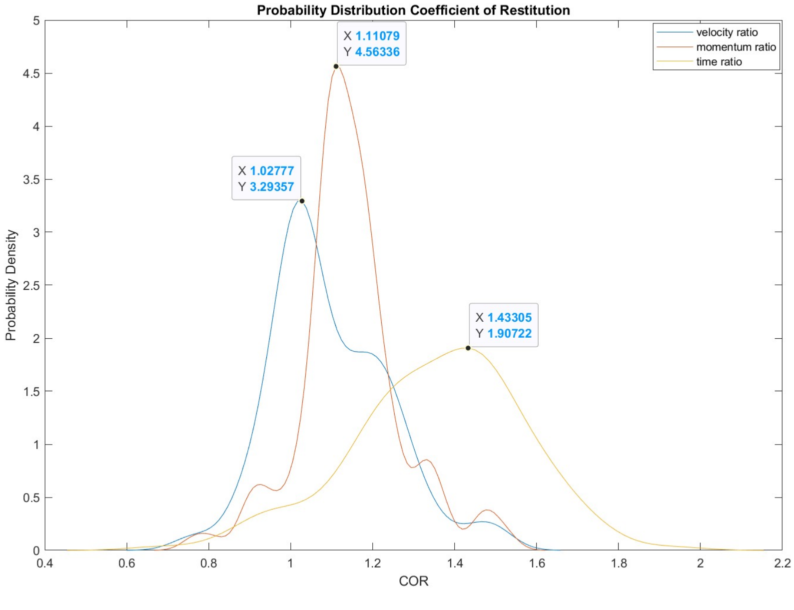

Figure 3.7: Probability distribution of the mean coefficient of restitution of the 10 impacts over the 180 tests, using the three different definitions

A first, immediate conclusion that can be drawn observing figure 3.7 is the marked difference between the coefficient of restitution defined as the ratio between the time periods $e = \frac{\tau_o}{\tau_i}$ and the other definitions; it is also possible to note the high mean value and flattened distribution. This conclusion was also supported by the results in Table 3.1.

The statistical test used to quantitively evaluate the similarity between the two distribution was the two-sample t-test. Even if the working hypothesis of the two-sample t-test were not strictly respected:

- the samples were independent only if it is considered that they come from different sensors, but were obtained simultaneously on the same test
- the samples had only approximately a normal distribution

Still, the method provided a quantitative measure that can be used to evaluate further refinements on the features extraction method: the objective of the improvement should be the increase of the p-value (currently at 0.7168) to prove the accordance between the force measurement and the acceleration one.

Null hypothesis	Result	p-value	Significance level
mean($e = \frac{v_o}{v_i}$)=mean($e = \frac{p_o}{p_i}$)	Not Rejected	0.7168	0.1
mean($e = \frac{\tau_o}{tau_i}$)=mean($e = \frac{v_o}{v_i}$)	Rejected	0.0033	0.1
mean($e = \frac{\tau_o}{tau_i}$)=mean($e = \frac{p_o}{p_i}$)	Rejected	0.0058	0.1

Table 3.1: Results of the two-sample t-test on the different coefficients of restitution

3.3 Statistical analysis

Once the desired impact characteristics were retrieved, a statistical analysis was performed to identify which parameters, out of the many selected in the experiment setup, mostly influenced some impact characteristics (namely the force peak, the coefficient of restitution and the impact duration).

The full factorial DOE already developed for the dataset [14] was analysed to find which parameters, and which combinations of parameters, had a larger effect on the mentioned characteristics.

Input parameters
Impact position
Hammer speed
Hammer tip material
Anvil plate material
Anvil insulator
Plate boundary conditions

Output parameters
Force peak
Impact duration
Coefficient of restitution $e = \frac{v_o}{v_i}$

The procedure followed can be resumed as:

- Calculate, for each characteristic (force peak, coefficient of restitution and impact duration), the effect produced by each parameter and by every possible combination of the parameters;
- Compare the values obtained with a half-normal distribution;
- Visually identify which parameters are more distant from the half-normal distribution: effects that lie along the straight line in the half-normal plot are likely random; effects that deviate significantly from the line are likely to be significant.

The parameters identified were selected as the most influential on the behaviour of each impact characteristic.

All the calculations were carried out using the Matlab Statistics Toolbox.

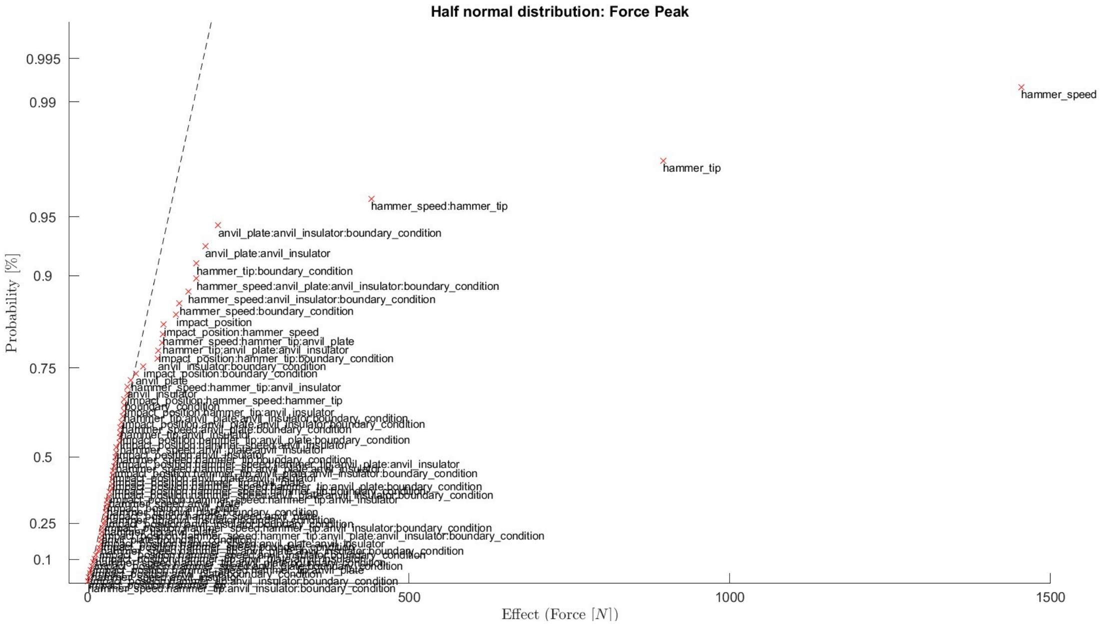

Figure 3.8: Half normal distribution and parameters for force peak

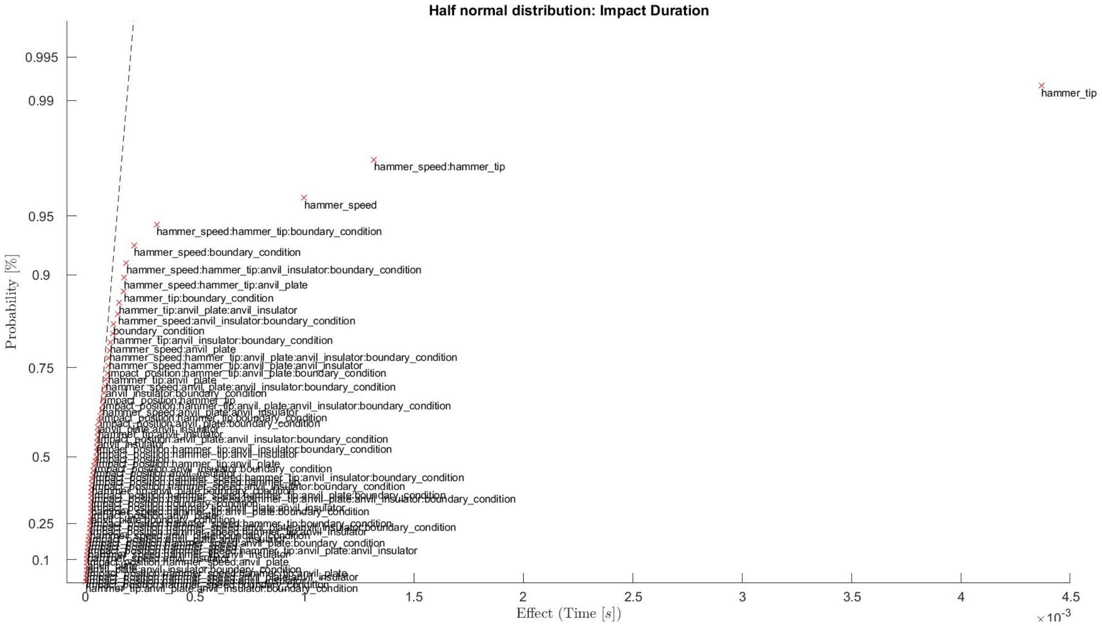

Figure 3.9: Half normal distribution and parameters for impact duration

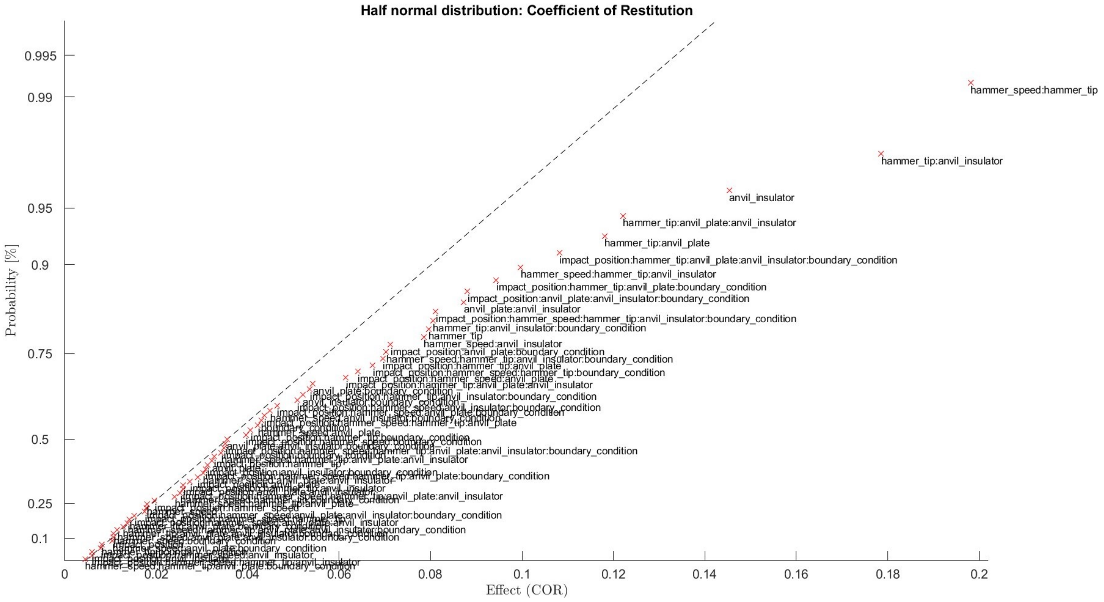

Figure 3.10: Half normal distribution and parameters for coefficient of restitution

As it can be seen, the hammer tip material and the hammer speed of impact have a large influence on the maximum force transmitted, the total impact duration and the coefficient of restitution; this last characteristic is also influenced by the presence of the anvil insulator and its material (not surprisingly, since the definition of COR as in equation 1.17 directly involves the properties of the impacted body). Boundary conditions seems to play a less relevant role, while the impact position contribution appears irrelevant.

Output parameter	Most influential input parameters
Force peak	Hammer speed Hammer tip
Impact duration	Hammer tip Hammer speed
Coefficient of restitution	Hammer tip Hammer speed Anvil insulator Anvil plate material

Although the results seem to be supported by what theory leads one to expect, caution in drawing conclusions must be taken, since in this section only a qualitative analysis based on the observation of the distribution was made; further discussion are made in Chapter 4.

3.4 Contact models simulation

After all the data of interest had been obtained, the force pulses defined by the contact models in the literature (see Chapter 1) were simulated by a MATLAB code that took as input all the different necessary parameters to calculate the force profiles in time.

The Tables 3.2 and 3.3 represent the material properties used (obtained from [14] and [20]) and the figure 3.12 shows an outline of the procedure followed by the MATLAB code.

	E $[GPa]$	ν	ρ $[\frac{kg}{m^3}]$	R $[mm]$
Aluminum	69	0.33	2700	30
Delrin	3	0.37	1410	30
Polyurethane	1	0.4	1100	15

Table 3.2: Hammer tips material properties

	E $[GPa]$	ν	ρ $[\frac{kg}{m^3}]$
Aluminum	69	0.33	2700
Steel	205	0.29	7850

Table 3.3: Plate and anvil material properties

A remark about the mass of the impacting object (m_1 in fig 3.12) provided as an input for the raised sine model, Hunt-Crossley model and Hunter model: this value was obtained dividing the maximum force and the maximum acceleration of each impulse $m = \frac{F_{max}}{a_{max}}$ (see figure 3.5a); the calculation yielded the result $m = 100$ g with a standard deviation of 7 g.

The total mass of the hammer used in the test 3.12 is 190 g , but not all the mass of the hammer contributes to the impact dynamics.

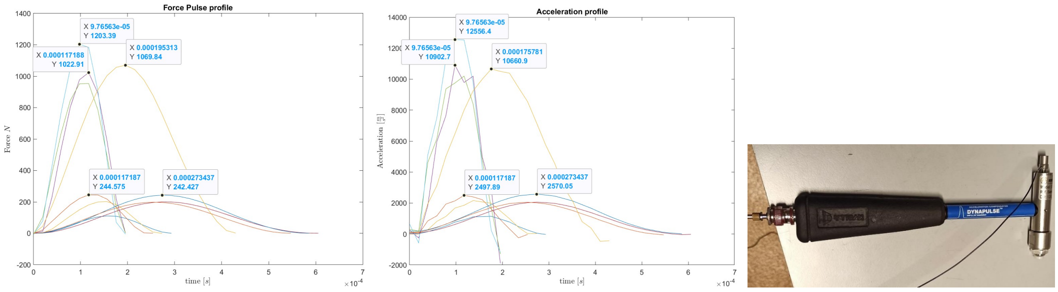

(a) Examples of force peaks **(b)** Examples of acceleration peaks **(c)** The hammer used

Figure 3.11: Estimation of the mass of the impacting part of the hammer used in [14]

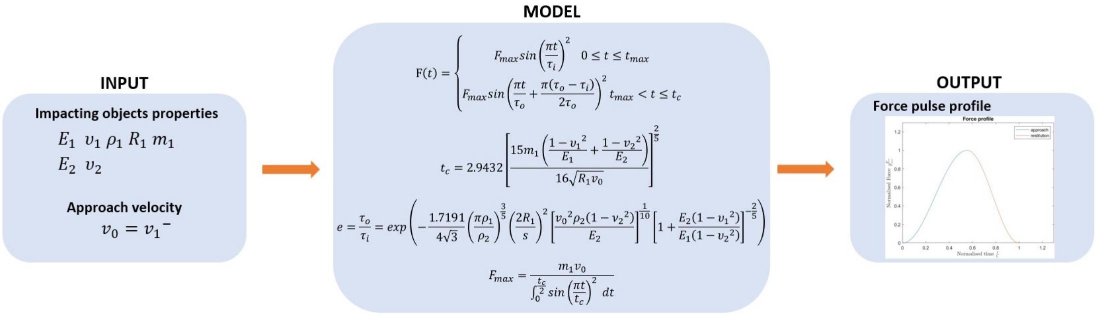

(a) Raised sine model

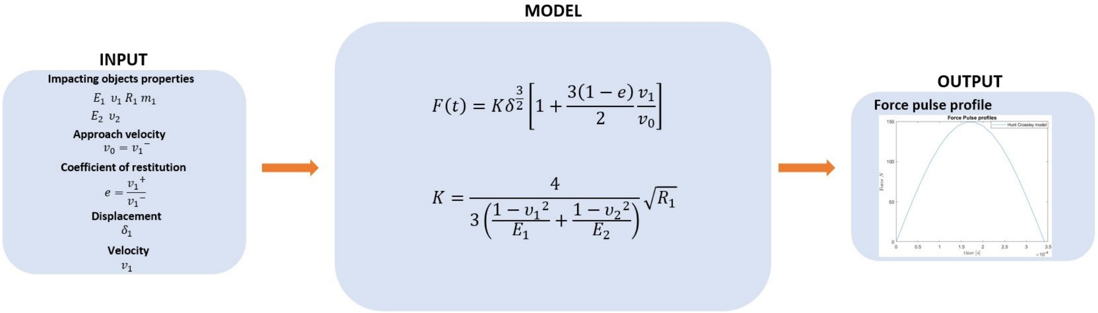

(b) Hunt-Crossley model

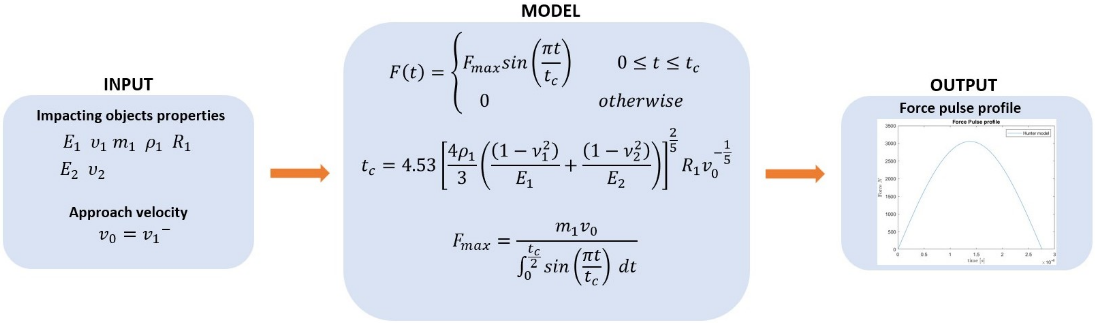

(c) Hunter model

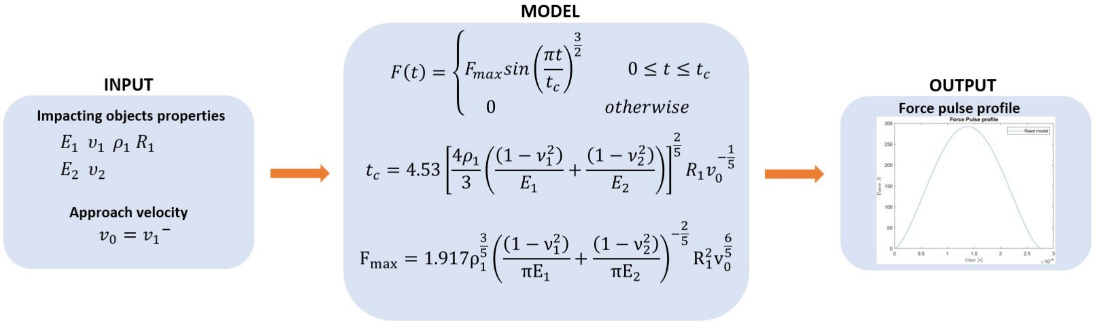

(d) Reed model

Figure 3.12: Input-output flowchart

3.5 Results

The different force pulses obtained were plotted on the same graph for each impact in the database to investigate which of the models better fit the force signal acquired.

The first conclusion that can be drawn is the inaccuracy of all the models in the representation of the impact between a soft material (the polyurethane tip) and the metal plate: the hypotheses of linear behaviour and elastic impact are deeply flawed in this case, thus the models referring to them deduce incorrect values.

This evidence should at least lead to caution in modelling the impulse produced by such material, if not to the avoidance of using it.

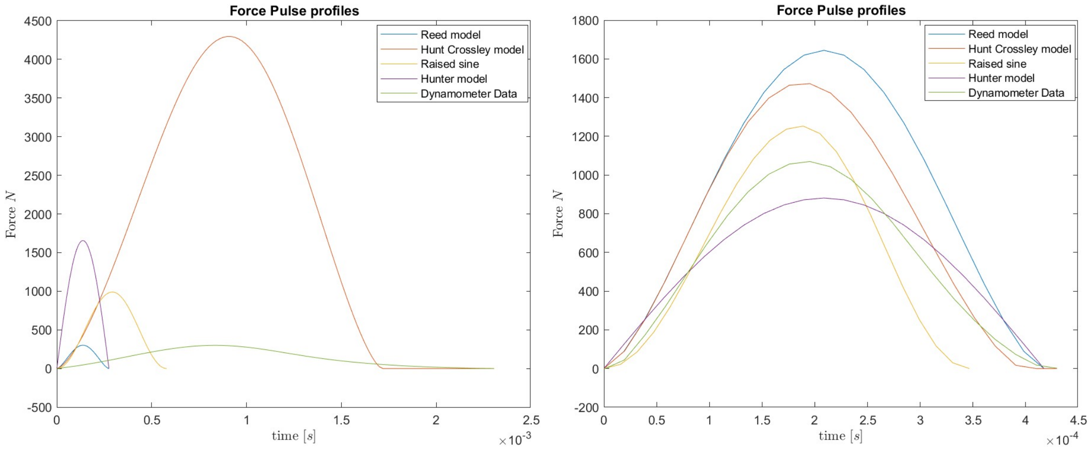

(a) Polyurethane tip

(b) Delrin tip

Figure 3.13: Differences between the models and data (green curve) of a polyurethane-aluminum impact and a delrin-aluminum impact

Another remark can be made about the amplitude of the force peak obtained by the models, that is consistently higher than the actual data obtained by the dynamometer; a plausible explanation lies in the definition of the mass of the impacting object: the value assumed relied on the mass of the hammer as measured in [14] and the considerations made in Chapter 3.4 regarding the relation between force and acceleration; actually, the mass of the whole hammer is not the mass of an equivalent free-moving object that impact the plate, due to the leverage effect, hand trajectory and operator influence.

A possible future improvement could be the determination of the exact mass equivalence between a hammer impact and a projectile-like impact.

To quantitatively evaluate the quality of the models, it was calculated a cost function between the force pulse obtained by the simulations and the real one; out of the many cost functions, the RMSE (Root Mean Squared Error) had been selected.

$$RMSE = \sqrt{\frac{1}{n}\sum_{i=1}^{n}(x_i - \widehat{x_i})^2} \tag{3.5}$$

Where n is the number of points evaluated, x_i is the force value calculated with the theoretical models and $\widehat{x_i}$ the actual force value obtained by the dynamometer.

Due to the demonstrated inaccuracy of all the models to simulate the force pulse performed by the polyurethane tip, in addition to a graph that represents all the RMSE results (figure 3.14), a graph in which all the polyurethane tip impacts were filtered out was used to draw conclusions about the various models (figure 3.15).

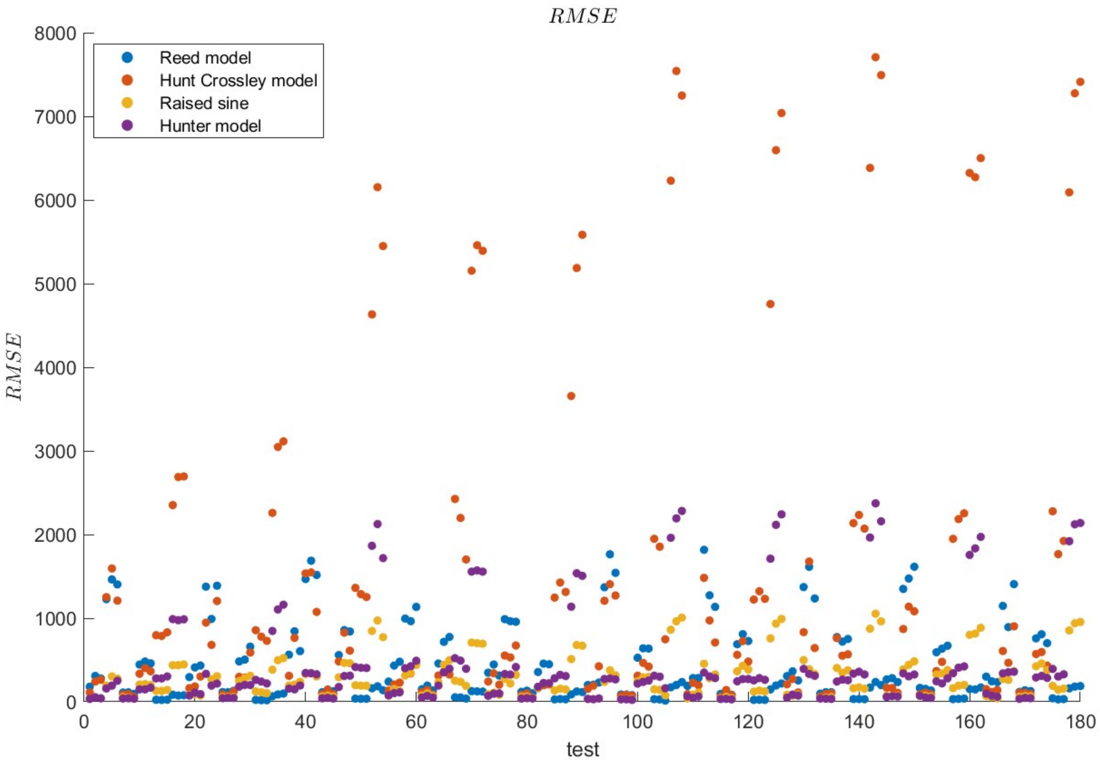

Figure 3.14: Mean Root Mean Squared Error over the 10 impacts for the 180 tests

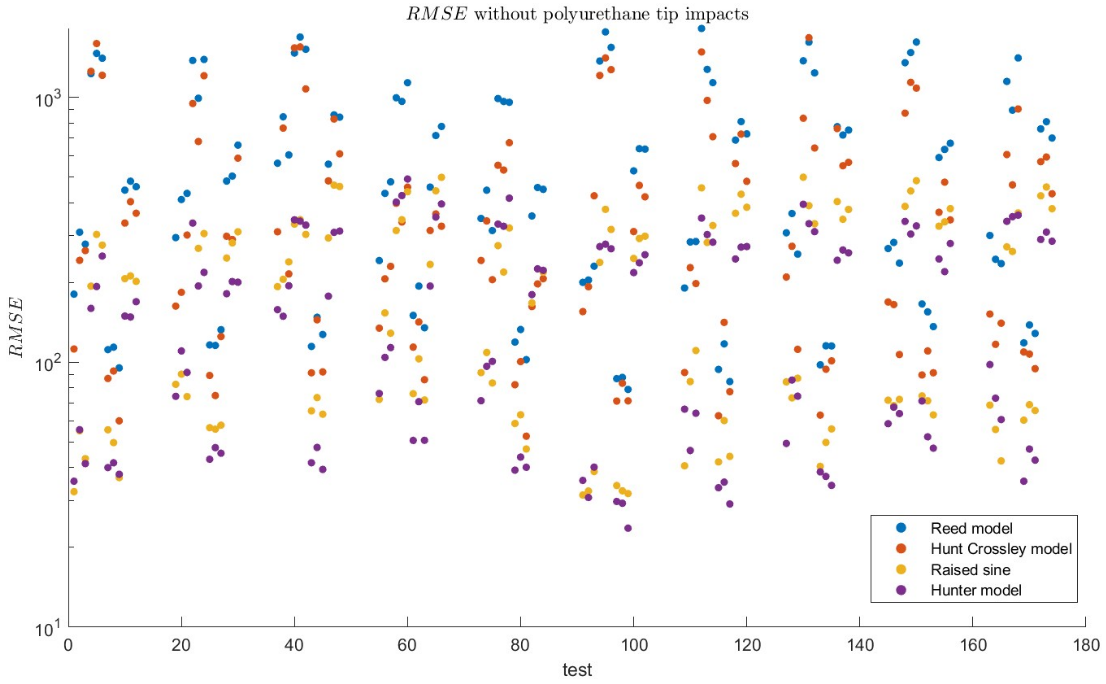

Figure 3.15: Semilog graph of the RMSE without the polyurethane tip results

The sum of all the mean RMSE across all the tests (filtered of the polyurethane tip impacts), normalised to the maximum of all the sums, was used as a score value to quantitatively evaluate the models:

$$score_i = \frac{\sum_{t=1}^{180} mean(RMSE)_i}{max\left(\sum_{t=1}^{180} mean(RMSE)_1, \sum_{t=1}^{180} mean(RMSE)_2, ..., \sum_{t=1}^{180} mean(RMSE)_n\right)} \tag{3.6}$$

Where $mean(RMSE)$ is the mean value over 10 impacts of the RMSE, t is the test number, i is the index that refers to the contact model and n is the total number of contact models analysed (4).

Hunter model	Raised sine model	Hunt Crossley model	Reed model
0.2847	0.3364	0.7222	1

Table 3.4: Normalised RMSE scores (lower values means better predictions)

The Hunter model was found to be the most accurate in almost all the tests, with a mean RMSE score almost always lower than other models, with a few exceptions in which the raised sine model scored better. The latter, used also in [6], was evaluated to be the second best model, with often comparable results with the Hunter model.

Chapter 4

Conclusions

The test bench analysed in this thesis satisfies the requirements of structural integrity and safety that were initially set: the assumed loading condition do not induce a stress state that would lead to criticality, and the analysis of the details according to European standards confirmed the validity of the design choices. The actual construction and acceptance of the structure have not been completed, so further discussions on its functioning in operation are postponed.

The results on the dataset studied confirm the validity of the raised sine impact model used in the article [6] to simulate the input in the predictive SRS model, and add an alternative model (Hertz model modified by Hunter) among the possible ones that can be used with comparable if not better results.

The analysis also highlighted the unreliability of every contact model analysed to correctly simulate the behaviour of impacts with a soft material as polyurethane. The conclusion that can be drawn is to avoid such materials in the bullet or hammer tip if an accurate prediction of the pulse profile is required, as in the case of [6].

Certain cautions must be made explicit about this section: the dataset analysed in this work and the method adopted to study it may be valid for hammer impacts with recorded accelerations and forces, but in the ideal use case of the test bench, a high-speed impact with a bullet is foreseen; the measurements possible in this type of impact are different: high-speed cameras can be used to record displacement and velocities, but it is not feasible to install a dynamometer on the bullet, hence force measurements cannot be obtained directly. Additionally, the behaviour of the different models proposed may change due to velocity related phenomena (plastic deformations) that may occur in presence of speeds of different order of magnitude ($\sim 1\,\frac{m}{s}$ for hammer impacts vs $\sim 50-100\,\frac{m}{s}$ for bullet impacts). Further improvements are necessary to tailor the results of the study on the actual test bench once it is available.

The results obtained in the statistical analysis performed on section 3.3 show that the most influential parameters on the impulse characteristics are lower than the total number of variables used for the experimental campaign and in accordance with the theoretical definitions of the parameters (e.g. coefficient of restitution influenced by impacting objects properties and speed); those conclusions can be confirmed by an additional test, often used in similar DOE studies [21]: the analysis of variance (ANOVA); this test can quantitatively evaluate the influence of the input parameters and is necessary to confirm or call into question the conclusions drawn.

The natural continuation of this work include the development of an air cannon that can be calibrated in parameters like speed, position of impact and material of the bullets, and the gathering of a sufficiently large database of impacts; those information can be used to further refine the predictive SRS model developed and subsequently use the model in the fine-tuning of the experimental setup, without the need for time-consuming iterations, on the required SRS.

Bibliography

[1] E. Mathieu and M. Roser. «Space Exploration and Satellites». In: *Our World in Data* (2022). https://ourworldindata.org/space-exploration-satellites (cit. on p. 2).

[2] Arianespace. *Ariane 5 User's Manual.* Issue 5 Revision 2. October 2016 (cit. on pp. 3, 8).

[3] ESA Requirements and Standards Division. *ECSS-E-HB-32-25A: Mechanical shock design and verification handbook.* Issue 1. July 2015 (cit. on pp. 4–7, 9–11).

[4] L. Viale, A.P. Daga, L. Garibaldi, and A. Fasana. «Numerical Modeling of a Pyroshock Test Plate for Qualification of Space Equipment». In: *European workshop on structural health monitoring* (2023) (cit. on p. 4).

[5] A.P. Daga, L. Viale, L.Garibaldi, A. Fasana, and S. Marchesiello. «Frequency domain convolutional model of a pyroshock plate for qualification of space equipment». In: *AIP Conf. Proc. 2872 120011* (2023) (cit. on p. 4).

[6] L. Viale, A.P. Daga, A.Fasana, and L.Garibaldi. «On pyroshock tests for aerospace equipment qualification: A comprehensive parametric model for the simulation and the design of pyroshock test facilities». In: *Int. J. Impact Eng. 180 104697* (2023) (cit. on pp. 4, 12, 14, 16, 34, 49, 50).

[7] C. Sisemore and V. Babuška. *The Science and Engineering of Mechanical Shock.* Switzerland: Springer Nature Switzerland AG, 2020 (cit. on p. 6).

[8] Junlan Li, Shaoze Yan, and Xuefeng Tan. «Dynamic-Envelope Analysis of Clamp-Band Joint Considering Pyroshock of Satellite Separation». In: *Journal Of Spacecraft and Rockets* (2014) (cit. on p. 9).

[9] J. Martin. «Development of a shock test facility for qualification of space equipment». In: 2012. URL: `https://api.semanticscholar.org/CorpusID:116248351` (cit. on p. 10).

[10] K. Ali and F. Juan. «JPL Tunable beam pyroshock simulation system». In: *Spacecraft and Launch Vehicle Dynamic Environments Workshop* (2007) (cit. on p. 11).

[11] V. L. Popov, M. Heß, and E. Willert. *Handbook of Contact Mechanics.* Germany: Springer-Verlag GmbH, 2019 (cit. on p. 13).

[12] G. C. McLaskey and S. D. Glaser. «Hertzian impact: Experimental study of the force pulse and resulting stress waves». In: *Journal of the Acoustical Society of America* (2010) (cit. on pp. 13, 36).

[13] K. H. Hunt and F. R. E. Crossley. «Coefficient of Restitution Interpreted as Damping in Vibroimpact». In: *Journal of Applied Mechanics* (1975) (cit. on pp. 14, 16).

[14] L. Viale and G. Tibert. «Description and Analysis of A Full Factorial Open-Access Dataset for Aerospace Shock Testing». In: *under review* (2024) (cit. on pp. 14, 15, 17, 34, 39, 42, 45, 47).

[15] C. Zener. «The intrinsic inelasticity of large plates». In: *Phys. Rev. 59* (1941) (cit. on p. 15).

[16] M. Rodrigues da Silva, F. Marques, M. Tavares da Silva, and P. Flores. «A compendium of contact force models inspired by Hunt and Crossley's cornerstone work». In: *Mechanism and Machine Theory* (2022) (cit. on p. 16).

[17] European Committee for Standardization. *Eurocode 3: Design of steel structures - Part 1-8: Design of joints.* 2005 (cit. on pp. 22, 25, 26, 29).

[18] J.E. Shigley R.G. Budynas and J.K Nisbett. *Shigley's mechanical engineering design.* New York: McGraw-Hill, 2011 (cit. on p. 27).

[19] R. Recht and T. W. Ipson. «The dynamics of terminal ballistics. Ballistic evaluation procedures for armored grille designs». In: *Denver Research Institute (Colorado Seminary)* (1962) (cit. on pp. 30, 31).

[20] «MatWeb: Online Materials Information Resource». In: (2024). https://www.matweb.com/ (cit. on p. 45).

[21] L. Viale, A.P. Daga, L.Garibaldi, S.Caronia, and I.Ronchi. «Books Trimmer Industrial Machine Knives Diagnosis: A Condition-Based Maintenance Strategy Through Vibration Monitoring Via Novelty Detection». In: *Proceedings of the ASME 2022, International Mechanical Engineering Congress and Exposition* (2022) (cit. on p. 50).